HEAT TRANSFER ASIAN RESEARCH
EDITOR-IN-CHIEF: *Professor William. M. Worek (Texas A&M University, USA)*
PUBLISHER- WILEY USA; ONLINE ISSN: 1523-1496
ACCEPTED DECEMBER 26TH 2018

COMPUTATIONAL STUDY OF HEAT TRANSFER IN SOLAR COLLECTORS WITH DIFFERENT RADIATIVE FLUX MODELS

Sireetorn Kuharat[1]
[1]*Aeronautical & Mechanical Engineering Department, School of Computing, Science and Engineering, Newton Building, University of Salford, Manchester, M54WT, UK.*
Email: S.Kuharat@edu.salford.ac.uk

O. Anwar Bég[2]
[3]*Aeronautical and Mechanical Engineering, University of Salford, Manchester, England, **UK.***
Email: gortoab@gmail.com, O.A. Beg@salford.ac.uk

Ali Kadir[3]
[3]*Aeronautical and Mechanical Engineering, School of Computing, Science and Engineering, Newton Building, Salford, M54WT, England, **UK.***
Email: A.Kadir@salford.ac.uk

MD. Shamshuddin[4*]
[4*]*Department of Mathematics, Vaagdevi College of Engineering, Warangal, Telangana, **India.***
Email: shammaths@gmail.com

***Corresponding author: Email: shammaths@gmail.com*
Orchid Number: 0000-0002-2453-8492

ABSTRACT
2D steady incompressible laminar Newtonian viscous convection-radiative heat transfer in a rectangular solar collector geometry is considered. The **ANSYS FLUENT** finite volume code (version 17.2) is employed to simulate the thermo-fluid characteristics. Extensive details of computational methodology are given to provide engineers with a framework for simulating radiative-convection in enclosures. Mesh-independence tests and validation are conducted. The influence of aspect ratio, Prandtl number (*Pr*), Rayleigh number (*Ra*) and radiative flux model on temperature, isotherms, velocity, pressure is evaluated and visualized in colour plots. Additionally, local convective heat flux is computed, and solutions are compared with the MAC solver for various buoyancy effects achieving excellent agreement. The P1 model is shown to better predict the actual influence of solar radiative flux on thermal fluid behaviour compared with the limited Rosseland model. With increasing *Ra*, the hot zone emanating from the base of the collector is found to penetrate deeper into the collector and rises symmetrically dividing into two vortex regions with very high buoyancy effect. With increasing *Pr* there is a progressive incursion of the hot zone at the solar collector base higher into the solar collector space and simultaneously a greater asymmetric behaviour of the dual isothermal zones.

Key words: *Solar collector enclosure; thermal convection; radiative heat transfer; aspect ratio, ANSYS FLUENT; finite volume; MAC computational algorithm.*

1. INTRODUCTION

The interest in sustainable and renewable energy systems has witnessed significant expansion in the 21st century. Both land-based (terrestrial) and space-based (astronautical) types of solar collector have attracted considerable attention. Solar thermal collectors utilize the incoming radiation by converting it directly into heat whereas

photovoltaics convert the radiation into electricity. Solar thermal systems therefore offer many desirable characteristics for propulsion, water and space heating.

Space solar power (SSP) collectors have multiple advantages over earth-based solar power plants. They receive more sun light, are unaffected by weather, free from the day-night cycle and expensive storage can be avoided [1-2]. The types of geometric designs which have been developed for spacecraft solar collectors are generally similar to those of terrestrial systems. They invariably feature an enclosure (cavity) in which the solar radiation initiates and sustains a circulation flow field. The thermo-physics inevitably involves *all three modes of heat transfer* (conduction, convection and radiation) although the individual contributions may vary with the particular design adopted, as elaborated by Kreith [3]. Several studies have confined attention to *thermal conduction* and radiation in spacecraft solar collectors including Yang et al., [4] who studied three-dimensional anisotropic conduction and a simple radiation network model for collectors in deep cold space. The key mechanism in fluid-based solar collector space power systems is however thermal convection and since gravitational forces near the earth and planetary bodies may still be significant, natural convection is of great interest in both gases or liquids. Fundamental studies of thermal convection in enclosures have been reported by many investigators. Many different geometries and boundary conditions have been considered. Although originally experimental studies were more popular, in recent years with the improved computer hardware and sophistication of numerical methods, computational simulation of enclosure thermal fluid dynamics has developed immensely. Motivation for these studies is not restricted to solar collectors only. Natural convection within closed square cavities with differentially heated isothermal walls feature prominently in nuclear reactors, energy efficient rooms, electronic cooling, crystal fabrication and also medical processing technologies. The buoyancy flows are considered complex due to the combination of transport properties of flow and the thermal fields. External flows are less complicated in comparison with internal flows. As a result of a large Rayleigh number (product of Prandtl and Grashof numbers), traditional boundary layer theory is used to make a simplified assumption for external flow problems, particularly in the region outside the boundary layer. In terms of natural convection, boundary layers form near the walls, however the region external to that is enclosed by the boundary layers and creates a core region. As the core is fully/partially surrounded by boundary layers, the core flow is yet to be determined from the boundary conditions which depends upon the boundary layer and in turn, is influenced by the core flow. There are major complexities associated with the interactions between boundary layer and the core flow since the intricacies at play tend to be due to the addition of more than one global core flow or the flow of sub regions like cells and layers which can be embedded into the core. A comprehensive review of many classical works in this

field has been presented by the premier researcher in this area, Ostrach [5]. In recent years many elaborate numerical simulations have been conducted. Aydm [6] conducted numerical investigations into the natural convection of rectangular enclosures heated from a single side and cooled from the ceiling using a stream function-vorticity formulation. A study into the influence of thermal boundary conditions on natural convection flows of a square cavity was presented by Basak et al., [7] who considered both uniformly and non-uniformly heated base wall and upper adiabatic wall conditions for (Rayleigh numbers between 10^3 and 10^5 and Prandtl numbers between 0.7 (air) and 10 (water). This choice of parameters is appropriate for the low gravity range which can be applied to a space solar collector. Bhargava et al., [8] employed both variational finite element and optimized finite difference methods to simulate thermo-solutal natural convection in a porous medium enclosure saturated with micropolar non-Newtonian fluid.

The above studies *neglected radiative heat transfer*. Solar energy is an important example of thermal radiation. To simulate radiative transfer, generally the integro-differential radiative transfer equation (**RTE**) is required. However, this is very challenging even with numerical methods and virtually intractable when other modes of heat transfer are considered simultaneously for complex geometries. Several studies of radiative, radiative-conduction and radiative-convective-conduction flows in solar collector enclosures have however been communicated. These include Su et al., [9] who used a ray tracing model to determine thermal efficiency of a compound parabolic collector. Khouki et al., [10] used the Radiation Element Method by Ray Emission Model (REM by REM) to simulate combined non-gray convective, conductive and radiative heat transfer in a glass solar collector glazing. Lee et al., [11] used a Monte Carlo algorithm and finite element analysis to simulate the radiative-conductive heat transfer in a direct solar thermal collector utilizing localized surface plasmon of metallic nanoparticles suspended in water. The effects of natural convection and radiation are present within the absorbing-emitting-scattering media, which is a detrimental problem for solar collector systems. Due to a range of industrial applications of heat transfer, the *combination of radiation and natural convection* has developed immense interest through numerous wide-spread research. Radiative heat transfer makes a significant contribution to CFD simulations. Hence, research into the numerical solution of fluid flow phenomena and heat transfer is essential. The numerical solutions generally employ some version of the Navier-Stokes equations (for Newtonian working liquids/gases) and an algebraic flux model for the radiative transfer equations (RTE). Many of these flux models which include the P1 flux model, Schuster-Schwartzchild two-flux model and Hamaker six-flux model have been reviewed in detail by Anwar Bég et al., [12-13]. Moufekkira et al., [14] were able to produce a study into the volumetric radiation and natural convection inside an isotropic scattering medium within a heated square cavity

using the hybrid thermal lattice Boltzmann method. They were able to discover that when modelling the surfaces of the enclosure walls as blackbodies, the maximum heat transfer rate was achieved. Mondal and Li [15] theoretically studied the effect of volumetric radiation on natural convection in a square cavity using a non-uniform lattice Boltzmann method (LBM) and a finite volume method (FVM) for the radiative term of the energy equation. Liu et al., [16] developed a two-dimensional numerical model with the Chandrasekhar discrete ordinate radiative method to compute the combined radiation and natural convection heat transfer in a grey, absorbing-emitting-scattering square cavity. For combined heat transfer, they were able to further evaluate the influences of Rayleigh number scattering phase function, aspect ratio of square cavity, scattering ratio and optical thickness. Rabhi et al., [17] used the Patankar SIMPLER algorithm and a Monte Carlo method to study the influence of surface radiation and number of partitions on the heat transfer and flow structures in an inclined rectangular enclosure, of aspect ratio of 4. They observed that net heat transfer in the enclosure is boosted with strong thermal radiation heat flux and reduced significantly with increasing the number of partitions. Anwar Bég et al., [18] implemented forward time central space (FTCS) finite difference and network electrothermal algorithms to investigate the combined radiation-convection-conduction in a porous medium annulus solar collector geometry. They deployed the Traugott P1-differential radiative transfer model and observed that increasing aspect ratio accelerates the axial and radial flow and furthermore enhances radiative moment of intensity, whereas greater optical thickness elevates the temperature and depresses radial radiative moment of intensity. Bouali et al., [19] used a boundary element approximation and a Monte Carlo method to analyze numerically the impact of surface radiation and inclination angle on thermal fluid characteristics in an inclined rectangular enclosure. Further studies include [20-23].

An inspection of the literature has identified that *relatively few investigations* have considered *simultaneously* the influence of different radiative flux models, fluid properties and enclosure aspect ratio on solar collector heat transfer. This is the motivation for the present study. We employ the SIMPLE algorithm available in the ANSYS FLUENT CFD code [24] and two radiative flux models, namely the Rosseland diffusion model [25] and the Traugott P1-differential radiative transfer model [26] to simulate radiative-convective two-dimensional steady flow in a rectangular enclosure. Excellent details of both radiative models (and numerous other models) are also available in [27-28]. Further details of applications of the Rosseland model in nonlinear thermal convection flows with radiation are provided in [29-30]. Numerical validation is performed with a Harlow-Welch marker and cell

code [31]. The influence of aspect ratio, Prandtl number (*Pr*), Rayleigh number (Ra) and radiative flux model on temperature, isotherms, velocity, pressure and streamline distribution is evaluated.

2. MATHEMATICAL MODEL

A square cavity containing a Newtonian viscous fluid (gas) is considered. The enclosure has a heated bottom wall of temperature 'T' at 413 Kelvin, unheated left and right walls at temperature 'T' at 385 Kelvin and an adiabatic top wall. Since gravity acts downwards, a buoyant flow develops as a result of thermally-induced density gradients.

There is no heat transfer though the top wall (adiabatic). No slip boundary conditions are assumed on all the walls of the cavity which are considered to be impermeable. The physical properties of the fluid are assumed to be constant. The physical model is visualized in Figure 1. The conservation equations for 2-D, steady, viscous, incompressible, laminar flow can be written in terms of primitive variables, *u*, *v*, *T*, and *p* as follows, including thermal buoyancy and radiative terms, as follows:

D'Alembert mass conservation (2-D continuity)

$$\frac{\partial u}{\partial x}+\frac{\partial v}{\partial y}=0 \tag{1}$$

x-direction momentum conservation

$$u\frac{\partial u}{\partial x}+v\frac{\partial v}{\partial y}=-\frac{1}{\rho}\frac{\partial p}{\partial y}+\nu\left[\frac{\partial^2 v}{\partial x^2}+\frac{\partial^2 v}{\partial y^2}\right] \tag{2}$$

y-direction momentum conservation

$$u\frac{\partial u}{\partial x}+v\frac{\partial v}{\partial y}=-\frac{1}{\rho}\frac{\partial p}{\partial y}+\nu\left[\frac{\partial^2 v}{\partial x^2}+\frac{\partial^2 v}{\partial y^2}\right]-g\left[1-\beta\left(T_\infty-T\right)\right] \tag{3}$$

Energy conservation

$$u\frac{\partial T}{\partial x}+v\frac{\partial T}{\partial y}=\alpha_m\left[\frac{\partial^2 T}{\partial x^2}+\frac{\partial^2 T}{\partial y^2}\right]-\frac{1}{\rho C_p}\frac{\partial q_r}{\partial y} \tag{4}$$

Here *u*, *v* denote *x*- and *y*-direction velocity components, *x* is the horizontal coordinate (aligned with base line of the enclosure), *y* is the transverse coordinate (aligned with the height of the enclosure), *T* is temperature, *p* is pressure, α is the thermal diffusivity and represents a measure of thermal inertia ($=\frac{K}{\rho C_p}$) where *K* is thermal conductivity of the working gas (W/mK), ρ is density kg/m^3) and c_p is the isobaric specific heat (J/kg K). When α is high, the heat moves fast as a fluid conducts heat quickly. Implicit in the secondary momentum equation (3) is the assumption of the so-called Boussinesq approximation of "weak" thermal convection i.e. density deviation from a mean value is only non-trivial in the equation of motion where it is incorporated in the buoyancy force

term which effectively couples the energy equation (4) with the secondary momentum equation (3). For small temperature drops in a flow the relation ρ (T) may be considered linear. The Boussinesq approximation correlates the coefficient of volumetric expansion of a medium β with the gravity acceleration g. Numerical values of β are usually small (water: $\beta = 1.5 \times 10^{-4}$, air: $\beta = 3.5 \times 10^{-3}$ at T = 273 K), therefore the density variation is taken into account only in those cases where it affects the gravitational forces. The term q_{rad} denotes the uni-directional radiative flux (W/m^2) which is imposed from the base of the enclosure acting vertically upwards. This is based on a flux model approach which circumvents having to solve the full equation of radiative transfer. ANSYS FLUENT provides five radiation models which enable radiative heat transfer simulation with or without a participating medium. These include the Chandrasekhar Discrete Ordinates (CDO) radiation model, surface-to-surface(S2S) radiation model, Rosseland radiation model, P-1 radiation model and Discrete Transfer Radiation Model (DTRM). Here we implement two different flux models, namely the Rosseland and P1 differential flux models. These both permit the propagation of radiation through the gaseous medium to be affected by absorption, emission and scattering processes, although they perform differently depending on the optical thickness of the gas. Radiative equilibrium is assumed in the simulations and the gas is also assumed to be gray [32]. We consider each model in turn:

P-1 Model

The general P-N model can be simplified as the P-1 radiation model [33]. The following equation is used for the radiation flux q_{rad} (if there are four terms used in the series):

$$q_r = -\frac{1}{3(\alpha+\sigma_s)\text{-c}\sigma_s}\nabla G \tag{5}$$

After introducing the parameter:

$$\Gamma = \frac{1}{\left(3(\alpha+\sigma_s)\text{-c}\sigma_s\right)} \tag{6}$$

Equation (6) simplifies to:

$$q_r = -\Gamma \nabla G \tag{7}$$

The transport equation for G is therefore:

$$\nabla \cdot \left(\Gamma \nabla G\right) - aG + 4an^2\sigma T^4 = S_G \tag{8}$$

This equation is solved in order to determine the local radiation intensity when the P-1 model is active. The following equation is a combination of Equations (7) and (8):

$$-\nabla \cdot q_r = aG - 4an^2\sigma T^4 \tag{9}$$

Due to the presence of radiation as a heat source (or sinks), the equation for $-\nabla q_r$ can be substituted into the

energy equation. DTRM (Discrete Transfer Radiation Model) is considered to be less accurate and commonly used in comparison to the P-1 model, which has several advantages. For the P-1 model, the general radiative energy equation can be approximated as the diffusion flux equation, allowing for a simpler calculation demanding less computational power from the CPU. The effect of scattering is included in the model. The P-1 model also works moderately well, even for high temperature-based applications, where optical thickness is large. Furthermore, the P-1 model can also be applicable for complex geometrical shapes of curvilinear coordinates. Nevertheless, there are some limitations where the P-1 model makes the assumption that all surfaces can diffuse. In this case, at the surface of the reflection of incident radiation is isotropic with respect to the solid angle. Hence the implementation makes the assumption of grey radiation. If the optical thickness is small, there may be a loss of accuracy, depending on the complicated geometrical shape. The P-1 model can also be observed to over-predict radiative fluxes near localised sinks or heat sources.

Rosseland Model Equation

Similar to the P-1 model, Equation (7) can be used to approximate the radiative heat flux vector inside a grey medium:

$$q_r = -\Gamma \nabla G \tag{10}$$

The Rosseland radiation model makes the assumption that the intensity is the black-body intensity at gas temperature, which differs from the P-1 model. The transport equation for *G* is computed by the P-1 model. Where, $G = 4\sigma n^2 T^4$ and n is known as the refractive index. By substituting this expression for *G* in Equation (10), gives:

$$q_r = -16\,\sigma\,\Gamma n^2 T^3 \nabla T \tag{11}$$

Since the radiative heat flux has the same form as the Fourier conduction law, it is possible to write:

$$q = q_C + q_r \tag{12}$$

$$q = -\left(K + K_r\right)\nabla T \tag{13}$$

$$K_r = 16\sigma\,\Gamma n^2 T^3 \tag{14}$$

In order to compute the temperature field, Equation (13) is used in the energy equation. The Rosseland model has great advantages over the P-1 model as the Rosseland model is able to develop a solution faster than the P-1 model. This is a due to the Rosseland model neglecting the incident radiation from the extra transport equation, which saves on the solving time and uses less memory. Regarding optically thick media, of an optical thickness exceeding 3, the model can be considered fairly accurate [34]. However, the Rosseland model is confined to

incompressible flow simulation i.e. cannot be used with the FLUENT density-based solver as it is being used and is only activated for the pressure-based solver.

Boundary conditions

The following primary and secondary velocity and temperature conditions are imposed at the four walls of the enclosure, in accordance with a number of published studies [19]-[21]:

$$\begin{aligned} &u(x,1)=1, u(x,0)=u=u(0,y)=u(1,y)=0, \\ &v(x,1)=v(x,0)=v(0,y)=v(1,y)=0, \\ &\frac{\partial T}{\partial x}(0,y)=-1, \frac{\partial T}{\partial x}(1,y)=0, \frac{\partial T}{\partial y}(x,0)=\frac{\partial T}{\partial y}(x,1)=0 \end{aligned} \tag{15}$$

3. ANSYS FLUENT FINITE VOLUME SIMULATIONS

Simulations of the heat transfer inside the solar collector cavity are separated into two cases: I) natural convection, (II) natural convection with radiation.

Case I: Natural convection

For the natural convection study, the problem considered is shown schematically in Figure 1**Error! Reference source not found.**. A square cavity has a heated bottom wall of temperature 'T' at 413 Kelvin, unheated left and right walls at temperature 'T' at 385 Kelvin and an adiabatic top wall. Since gravity acts downwards, a buoyant flow develops as a result of thermally-induced density gradients. The working fluid has a Prandtl number of approximately 0.71, and a Rayleigh number based on '*L*' is $5x10^5$. To validate the solution, the test case from Basak et al., [7] is used. The values of physical properties and operating conditions (e.g. gravitational acceleration) have been adjusted to yield the desired Prandtl, Rayleigh and Planck radiative-conductive numbers. The fluid properties are adjusted (fluid thermal conductivity) in order to vary the Pr number to 0.3, 0.7 and 1.4, whilst the Rayleigh number is kept constant at 1000. The main fluid properties inside the square cavity are shown in Table 1. In order to vary gravity, the Rayleigh number can be adjusted from 100 - 10,000,000 whilst keeping Prandtl number constant at 0.7.

The last case is conducted by changing the aspect ratio of the geometry to aspect ratios 'AR' equal to 0.5, 1 and 2 as shown in Figure 2. With regard to the enclosure (cavity) top wall, the classical no slip boundary conditions are assumed and furthermore the wall is solid i.e. no mass flux possible (impermeable). There is no heat transfer through this wall since *adiabatic* conditions are imposed. Obviously in this case the radiative flux term in the energy conservation equation (4) vanishes.

Case II: Natural convection with radiation

The study involving natural convection with the inclusion of radiation, considers a working fluid in a square cavity with a Prandtl number of approximately 0.71 and a Rayleigh number based on 'L' of $5x10^5$. Natural convection is similar to the natural convection with radiation, however the only difference is the medium contained within the cavity, which is assumed to be absorbing and emitting. In this case therefore the radiant exchange between the walls can be attenuated by absorption and augmented by emission in the medium where all walls are black. The Planck number $\left(k / 4\sigma L T_0^3\right)$ is 0.02 and measures the relative importance of conduction to radiation; here $T_0 = (T_h + T_c) = 2$.

3.1 ANSYS Methodology

As with general purpose commercial CFD packages, ANSYS FLUENT provides a sophisticated user interfaces to input parameters and to examine the results. It operates with three distinct phases- pre-processor (geometry), Solver (numerical solution of the conservation equation) and post-processor (visualization of the results). An overview of the FLUENT CFD process is shown in Figure 3 below:

3.1.1 Pre-processing-Geometry and Meshing

Two-dimensional, single-phase laminar flow is considered. The physical model is first simulated as a square cavity with aspect ratio of 1. The geometry model was produced by using the sketching tool which was then dimensioned to the specification's ratio of 0.5, 1 and 2. The 2D "Surface Body" was created from the sketch as shown in Figure 4**.** The software allows for a multitude of mesh techniques using structured grids, unstructured grids or a combination. In addition, meshed models can consist of quadrilateral cells (used in 2D), triangular cells (used in 2D) and hexahedral, tetrahedral, polyhedral, wedge cells, or pyramid (or a combination of these are used in 3D). The meshing process for this study of laminar flow inside the cavity is performed using structured meshes. The structured meshes used quadrilaterals as this type of element is commonly used in a simple geometry to save on the setup time. In term of computational expense, a characteristic of quadrilateral elements is greater economy for situations that permit a much larger aspect ratio than triangular/tetrahedral cells. A large aspect ratio in a triangular/tetrahedral cell will invariably affect the skewness of the cell, which is undesirable as it may impede accuracy and convergence. The mesh convergent study is an additional method of analysing ways of improving the accuracy of the simulation, therefore the number of elements used in the simulation is increased until it reaches convergence. The numbers of nodes and elements of each mesh (grid) numerical experiment case are shown in

Table 2. Meshes are depicted in Figure 5. Table 3 provides the details for the five cases of mesh grids studied with element numbers and nodes and discretization characteristics in the x and y directions.

3.1.2 Physical boundary condition specification

The boundary conditions are specified on each edge of the computational domain (2-D flows). Appropriate boundary conditions are required to obtain an accurate CFD solution. The cavity is heated from the bottom wall to a constant temperature and the unheated cold walls on both sides will be of a constant temperature. The temperature difference between the hot and cold walls are kept constant at 20 Celsius. There is no heat transfer through the top wall since the top wall is adiabatic. No slip boundary conditions are assumed on all the walls of the cavity and considered to be impermeable. After validating the result, the fluid properties are varied according to the different case of investigation which is explained in more detail subsequently.

3.1.3 Solving

To conduct natural convective heat transfer simulation in the enclosure, the double-precision versions of the CFD code were carefully chosen. This is due to the conjugate problems involving high thermal-conductivity ratios, convergence and accuracy which are impaired with the use of the single precision solver due to the inefficient transfer of boundary information. As the name suggests, the double precision tool selects the double-precision solver. To note, double-precision solver contains floating-point numbers that are referenced using 64-bits whereas, the single-precision solver uses only 32-bits for every floating-point number. With the addition of the extra bits, this has a strong effect on the range of magnitudes represented and the precision of the tool. Using double precision also takes a toll on the computer memory resources available as elaborated by Koenig [35]. To begin the discretisation process, the Navier-Stokes equations, heat transport forced convection equations and Radiative Intensity Transport Equations (P1 model, Surface to Surface model) must be turned on in the software. To enable the function of natural convection in the simulation, the Boussinesq model must be activated within the 'define material' function which will aid in calculating the density. Upon the activation of the Boussinesq model, the thermal expansion parameter can be inputted as shown in Figure 22**.** Gravity can be enabled to allow for the effect of gravity on the simulation, this can be accessed in the operating condition. This is a very crucial step to enable the effect of natural convection. If the Boussinesq model is not active, then the simulation will act under *pure forced convection*. Next all the conservation equations mentioned above are solved using the SIMPLE algorithm. This can also be referred as the projection method. The '*u', 'v', 'p'* and *"T*" fields must be solved separately. The constraint of the mass conservation of the velocity field can be solved in the projection method using a pressure/pressure-correction equation. The pressure equation is a derivation of the momentum and continuity

equations, corrected using the pressure for the velocity field to satisfy the continuity. As a result of the coupled nature and non-linearity of the governing equations, developing a solution includes iterations where complete governing equations can be solved continually until reaching a converged solution. Coupled and segregated algorithms are two pressure-based solver algorithms used in FLUENT [36]. This algorithm is able to obtain the pressure field by developing a relationship between the pressure and velocity corrections in which enforces the mass conservation. By substituting the flux equation into the discrete continuity equation, the SIMPLE algorithm can be developed to acquire a discrete equation to allow pressure correction in the cell. Using algebraic multigrid (AMG) method, the pressure-correction equation may be solved. Upon achieving a solution, the cell pressure and the face flux are then corrected. The sum of a CFD solution will decrease through progressive iterations, however it will never reach an identical value of zero. And the residual is one of the measurements of how much a solution to a given transport equation deviates from. The average residual associated with each transport equation is monitored in order to help determine when the solution has converged. For this simulation, large numbers of iterations are required to meet the final solution, in addition the residuals can be reduced by numerous orders of magnitude. The robust SIMPLE methodology is summarized in Figure 6. The general methodology is given in Figure 7. SIMPLE also employs a second order upwind numerical method. When the computational domain has a non-unity aspect ratio this will require a very high degree of accuracy. Hence, the second order upwind method is used for velocity and pressure calculations. To apply second-order accuracy, the multidimensional linear reconstruction approach to compute the quantities at the cell faces are explained by Barth and Jespersen [37]. Thus, the cell faces accuracy is achieved through the use of Taylor series expansion of the cell-centred solution about the cell centroid. The following expression is used to compute the face value 'φ_f' for a second-order upwind method.

$$\phi_f, SOU = \phi + \nabla\phi.\vec{r} \tag{16}$$

The gradient '$\nabla\varphi$' eventually reaches a limit so that no new maxima or minima are introduced. Second-order upwind is available in the pressure-based and density-based solvers Barth and Jespersen [36] (Barth and Jespersen, 1989).

There are numerous factors that can prevent a simulation from reaching convergence i.e. complexity of the flow physics, a geometry requiring a large number of computational cells and excessive conservative under-relaxation. On certain occasions, it is difficult to judge whether a result has achieved convergence. There are a variety of modelling techniques and numerical controls to maintain stability and to improve convergence other than conducting a mesh convergence study. Using the residual definitions is very useful for certain problems, on the

other hand it can also be misleading for other types of problems. It is recommended to examine residual levels along with related integrated quantities and hence for this case, the heat transfer coefficient. However, for non-complex problems the default convergence criterion should be sufficient.

The minimum scaled residuals are required to decrease to 10-3 for most equations excluding the P-1 and energy equations, which are used in this simulation where the criterion is 10^{-6} in this case. Figure 8 shows the residual monitoring output in the present computations.

3.1.3 Post-Processing

Once the solution has converged, flow field variables such as velocity stream line function and temperature are automatically plotted and analysed graphically. Since a fixed temperature condition is applied at the wall for this study, the wall heat flux (q) is directly computed as follows:

$$q = h_f \left(T_w - T_f \right) + q_r \tag{17}$$

The fluid-side heat transfer coefficient computed is based on the local flow-field conditions i.e. temperature and velocity profiles. The fluid side heat transfer at walls is computed using Fourier's law applied at the walls. The following discrete form is used:

$$q = k_f \left(\frac{\partial T}{\partial n} \right)_{wall} \tag{18}$$

Heat transfer to the wall boundary from a solid cell is computed as:

$$q = \frac{ks}{\Delta n} \left(T_w - T_s \right) + q_r \tag{19}$$

Here k_S designates the thermal conductivity of the solid, T_S is the local solid temperature and Δn denotes the distance between wall surface and the solid cell centre.

3.1.4 Grid Sensitivity Analysis

For the grid sensitivity analysis, the wall heat flux is compared for different grid density at x=0.5, y=0. The details of different meshes are represented in the

. The notation ϕ_h is adopted for the solution of the finest mesh. The subsequent meshes are all denoted with respect to the finest mesh. The next grid size has cell dimension doubled in both directions, hence the notation ϕ_{2h}.

It can be shown that the grid is approximately defined by:

$$\varepsilon_h^d \approx \frac{\phi_h - \phi_{2h}}{2^a - 1} \tag{20}$$

Here a is the order of the scheme and given by:

$$a = \frac{\log\left(\frac{\phi_{2h} - \phi_{4h}}{\phi_h - \phi_{2h}}\right)}{\log(2)} \tag{21}$$

In both equations (20), (21) the 2 refers to the increase in dimension of the mesh. Eqn. (20) indicates that a minimum of three meshes are required to determine the discretization error. In order to prevent a calculation error from the logarithm of a negative number, the three solutions must be monotonically converging. The theory of Richardson extrapolation implies that solutions from the finest mesh can be added to the discretization error found in equation (21) to attain an approximate grid independent solution. In equation from this can be states as:

$$\Phi = \phi_h - \varepsilon_h^d \tag{22}$$

The results from the grid sensitivity analysis are shown in Table 4 and Figure 9 below. Figure 9 illustrates the grid sensitivity analysis. The largest elements used in case one can be considered as a coarse mesh with 525 elements. When the size of the elements is reduced by half, the graph shows a significant decline indicating that the simulation is not convergent. Even though the difference between these two results is very small, nevertheless the natural convection is very sensitive to heat flux and cannot be ignored. The next part of the grid dependence study covers cases three, four and five. Upon observation of cases four (22110 elements) and five (33750 elements), these cases used finer meshes, where the difference between the two values are infinitesimal and hence considered negligible. This shows that the simulation is convergent by case four with 22110 elements. This grid dependent study provided an appropriate grid size, used in case four, to be selected for the proceeding part of the study to achieve the most accurate result with minimum number of elements.

3.1.5 Validation with study of Basak et al., [7] *(*Basak et al., 2006)

As mentioned in the literature review Basak et al., [7](Basak et al., 2006) investigated the steady laminar natural convection flow inside a square cavity, which was uniformly and non-uniformly heated on the bottom side of the wall. However, it is possible to compare with streamline function and temperature patterns. The comparisons are given in Figures 10-11. Very good correlation is clearly observed. This analysis was selected as a benchmark from the published literature for validation and corresponds to an aspect ratio of unity, Pr = 0.7 and Ra=10^3 as shown in Figure 12. Since [17] (Basak et al., 2006) employed dimensionless variables, it is not feasible to verify against their normalized solutions.

4. VALIDATION WITH MARKER AND CELL METHOD

The primitive governing partial differential equations (1) -(4) subject to the imposed dimensionless boundary conditions (15) have also been solved with a MAC (marker and cell) method which is an implicit scheme using a

staggered grid. The velocity–pressure gradient causes strong coupling in the continuity and the projection method is implemented for the primary and secondary momentum equations. The special finite difference scheme introduced by Harlow and Welch [31] is implemented to minimize the numerical diffusion for the advection terms. In the MAC approach although we consider viscous flow, viscosity is not actually required for numerical stability. Cell boundaries are labelled with half-integer values in the finite difference discretization. The marker particles do not participate in the calculation. Here we elaborate on the numerical discretization procedure. Based on the weak conservative form of the steady-state two-dimensional Navier-Stokes equations and heat conservation equation as defined by equations (1) -(4), we implement a grid meshing procedure using the following notation at the centre of a cell (see Figure 13).

$$u_{i-1/2,j} = \frac{1}{2}\left[u_{i-1,j} + u_{i,j}\right] \tag{23}$$

Applying to the x-direction momentum conservation eqn. (2) we have:

x-momentum Discretized Advection term:

$$\frac{\partial(uu)}{\partial x} = \frac{uu1 - uu2}{\Delta x} \tag{24}$$

where

$$uu1 = \left[\frac{1}{2}\left(u_{i,j} + u_{i+1,j}\right)\right]^2$$
$$uu2 = \left[\frac{1}{2}\left(u_{i-1,j} + u_{i,j}\right)\right]^2 \tag{25}$$

x-momentum Discretized Advection term:

Similarly, we have:

$$\frac{\partial(uv)}{\partial y} = \frac{uv1 - uv2}{\Delta y} \tag{26}$$

where

$$uv1 = \frac{1}{2}\left(u_{i,j} + u_{i,j+1}\right).\frac{1}{2}\left(v_{i,j} + v_{i+1,j}\right)$$
$$uv2 = \frac{1}{2}\left(u_{i,j} + u_{i,j-1}\right).\frac{1}{2}\left(v_{i,j-1} + v_{i+1,j-1}\right) \tag{27}$$

The following central difference formula are used for the second order derivatives:

$$\nabla^2 u = \frac{\partial^2 u}{\partial x^2} + \frac{\partial^2 u}{\partial y^2}$$
$$\nabla^2 u = \frac{u_{i-1,j} - 2u_{i,j} + u_{i+1,j}}{\Delta x^2} + \frac{u_{i,j-1} - 2u_{i,j} + u_{i,j+1}}{\Delta y^2} \tag{28}$$

Applying to the y-direction momentum conservation eqn. (3) we have:

y-momentum Advection term:

$$\frac{\partial (vu)}{\partial x} = \frac{vu1 - vu2}{\Delta x} \tag{29}$$

Here the following notation applies:

$$\begin{aligned}
uv1 &= \frac{1}{2}\left(u_{i,j+1} + u_{i,j}\right).\frac{1}{2}\left(v_{i,j} + v_{i+1,j}\right) \\
uv2 &= \frac{1}{2}\left(u_{i-1,j+1} + u_{i-1,j}\right).\frac{1}{2}\left(v_{i,j} + v_{i-1,j}\right) \\
\frac{\partial (vv)}{\partial y} &= \frac{vv1 - vv2}{\Delta y} \\
vv1 &= \left[\frac{1}{2}\left(v_{i,j+1} + v_{i,j}\right)\right]^2 \\
vv2 &= \left[\frac{1}{2}\left(v_{i,j-1} + v_{i,j}\right)\right]^2
\end{aligned} \tag{30}$$

The central difference formula for the Laplacian operator is given by:

$$\begin{aligned}
\nabla^2 v &= \frac{\partial^2 v}{\partial x^2} + \frac{\partial^2 v}{\partial y^2} \\
\nabla^2 v &= \frac{v_{i-1,j} - 2v_{i,j} + v_{i+1,j}}{\Delta x^2} + \frac{v_{i,j-1} - 2v_{i,j} + v_{i,j+1}}{\Delta y^2}
\end{aligned} \tag{31}$$

There is a slight modification needed in the *y*-momentum equation due to the addition of a new term. Therefore, this term must be included in the discretized equation. It is further noteworthy that the temperature term T is co-located such that it coincides with velocity before using it in the above equation to account for the staggered grid. Modern variants of the MAC method utilize the conjugate gradient schemes which solve the Poisson equation. Further details are provided in Basak et al., [7]. Extensive comparisons have been conducted and visualized in Figure 14 for the local convective heat flux along the base wall (i.e. heated wall) in the enclosure Excellent correlation was achieved for the test case of Ra = 10^7 (uppermost curve) corresponding to air (Pr =0.7) and an aspect ratio of 1. Confidence in the ANSYS simulations is therefore very high. With increasing Rayleigh number there is a substantial elevation in convective heat flux along the heated wall surface. The flux is minimized at the mid-way point which agrees with the findings of Taoufik *et al.* [38] who used a lattice Boltzmann method. Generally symmetric distributions are achieved about this minimal point (trough) with flux climbing symmetrically from this point with axial distance (x) and peaking at the walls of the enclosure. This concurs with the cooling effect observed in the temperature plots (blue zones) as reported by Taoufik and Ridha [39].

5. CFD SIMULATION RESULTS

We now present detailed simulations obtained by ANSYS FLUENT for different thermal fluid characteristics in the solar collector enclosure. All computations are visualized in Figures 15-25. We consider both Case I and Case

II as explained earlier in section 3. In each Case we consider first the influence of Rayleigh and Prandtl numbers, then aspect ratio.

Case I: Natural Convection of Varying Rayleigh Numbers

Computations are plotted in Figures 15-16. The computations show that with increasing Rayleigh number i.e. buoyancy effect there is a distortion in the temperature fields. Moving from *Ra =100 to Ra = 1000* (ten times greater thermal buoyancy force) the lower heated zone near the base wall is expanded significantly. Heat flux penetrating the solar cell is enhanced.

High temperatures spread upwards and there is a contraction in the coolest zones in the vicinity of the upper wall. With subsequent enhancement in Rayleigh number the parabolic profiles which dominate the regime at lower Rayleigh numbers (*Ra* = 100, 1000) are eliminated and a sand-glass thermal field structure emerges. The highest temperature zone grows from the centre of the base wall extending deeper into the cell. The warmer zones (green) expand laterally to span most of the solar cell space, demonstrating more homogenous energy distribution in the regime. The cooler zones (blue) clearly contract and are restricted to the lateral walls. The strongest buoyancy case therefore achieves the desired effect, a more even allocation of heat through the body of the cell. Evidently there is a critical Rayleigh number between 1000 and 10,000 where the temperature field topology is dramatically altered. At *Ra* = 10,000 the dual structure is synthesized and begins to emerge symmetrically. However, it does not form completely. As Rayleigh number is increased, the dual thermal field structure computed in the solar cell evolves considerably although it is only truly formed at the highest Rayleigh number (Ra =10,000,0000). The temperature hot zone at the base of the wall is progressively dwindled as heat is circulated through the enclosure. The thin blue slices at the lateral walls contract significantly indicating that heat is dispersed much more evenly through the enclosure. Buoyancy therefore is a substantial factor influencing the transport of heat within the enclosure. The isotherm plots corresponding to the temperature plots are presented. The dual circulation structures are largely unchanged from Ra =1000 to 100,000. At these lower Rayleigh numbers stronger intensity is observed at the core of the left circulation zone compared with the right one. The magnitudes of the two zones are also approximately the same. However, with further increase in Rayleigh number, as greater buoyancy effect is imposed, the two circulation zones move initially upwards strongly and then eventually strongly dissimilar trends are observed at Rayleigh number of 10,000,000. At this maximum value the left zone becomes skewed to the top left and lower half. Conversely the right zone is split into two smaller zones. The impact of buoyancy on isotherms is similar to the results reported by Oh et al., [40] and Paroncini and Corvaro [41].

Case II: Natural convection with varying Prandtl numbers

Now we discuss the impact of Prandtl number which is illustrated in Figures 17-18. Prandtl number is the heart of all thermal convection heat transfer analysis and design. It is not merely a scaling parameter but in fact a property of a fluid at a given temperature and pressure. It expresses the ratio of momentum diffusivity to energy diffusivity i.e. how fast momentum is conveyed compared to how fast heat is transported in a fluid. An increase in *Pr* from 0.3 (Nobel gases) through 0.7 (air) to 1.4 (gaseous ammonia) allows different solar collector fluids to be studied. The temperature also decays quickly for large values of Prandtl number. The thermal boundary layer thickness is similarly the distance from the body at which the temperature is 99% of the temperature found from an inviscid solution. The ratio of the two thicknesses is dictated by the Prandtl number. For Prandtl number of unity, both boundary layers are of the same thickness i.e. order of magnitude. However, when Prandtl number exceeds unity, the thermal boundary layer is thinner than the velocity boundary layer. Generally, higher *Pr* fluids will have relatively low thermal conductivities which will suppress thermal conduction heat transfer *from the wall* and reduce thermal boundary layer thickness, resulting in lower temperatures in the regime. Smaller values of *Pr* are equivalent to increasing thermal conductivities, and therefore heat is able to diffuse away from the walls more rapidly than for higher values of *Pr* . Hence in the case of smaller *Pr* the boundary layer is thicker and the rate of heat transfer *to the wall* i.e. Nusselt number is reduced. This creates a deeper red zone with greater thermal energy localized at the base of the solar cell for *Pr* =1.4 compared with *Pr* = 0.3. The exploration of these fluids is noteworthy. Nobel gases are less likely to ignite i.e. explode. On remote missions this is a critical factor to be noted, which has important implications in solar collector performance. The noble gases show extremely low chemical reactivity. Noble gases are commonly used in lighting because of their lack of chemical reactivity. Argon, mixed with nitrogen, is used as a filler gas for incandescent light bulbs. Krypton is used in high-performance light bulbs, which have higher color temperatures and greater efficiency, because it reduces the rate of evaporation of the filament more than argon. Since thermal radiation and light are obviously produced by the sun, avoiding reactivity is essential in deep space operations where solar flux is tremendous. However, a weaker performance for dispersing thermal energy results with the Nobel gas compared with a more reactive gas (ammonia, Pr =1.4). Hence the solar collector designer must select the working fluid very carefully. In terrestrial applications Ammonia being an environmentally friendly gas reduces the effect of ozone layer depletion. In space applications ammonia is typically doped with non-reactive particles which stabilize it to light effects avoiding ignition, sparking etc. In spacecraft applications, Ammonia (NH_3) can be decomposed and later recombined in a repeating thermochemical energy storage cycle which allows selective storage of energy and the excellent facility for storing it for longer periods until required. Ammonia therefore has several advantages over other working

fluids in direct absorber solar collectors. Significantly deeper penetration of the solar flux into the entire cavity is achieved with higher Prandtl number fluids. A more symmetric and stable dual bolus structure is also computed for the isotherms with largest Prandtl number. Local convective flux at the wall is also plotted in Figure 19. It is observed to be decreased with greater Prandtl number. Again, this has implications for the Nusselt number. Higher *Pr* implies greater thermal conductivity of the fluid and this encourages heat transport from the wall into the solar collector. This results in decreasing Nusselt number and local convective flux at the wall.

Case III: Natural convection with aspect ratio variation

To complete the evaluation of Case I we examine the influence of the geometric parameter i.e. aspect ratio. Visualizations are depicted in Figures 20-21. Significant modification arises in the temperature distributions with a decrease in aspect ratio.

When the solar collector has AR = 2 (width is twice the height) the higher temperature ascends throughout the solar collector and reaches much higher than for lower aspect ratio (AR = 1 corresponds to a square and AR = 2 to a slender rectangle with double the height compared to the width). The allocation of heat through the solar collector is therefore strongly modified by a simple change in the relative dimensions of the walls. Colder zones are progressively enlarged and dominate the upper half space of the solar collector when AR = 1 and more so for AR = ½. The isotherms are also significantly altered. The symmetric dual structure which covers the entire solar collector space for AR = 2 is progressively displaced towards the lower hot wall as AR is increased. There is therefore a bias in heat transferred to the lower wall with greater aspect ratio, an undesirable characteristic of solar collectors - see Duffie and Beckman [42]. Of course, these simulations are all restricted to air and a relatively low Rayleigh number (100). Local convective flux as shown in Figure 22, is modified with AR but less dramatically than via the Rayleigh or Prandtl number. Convective flux (and therefore Nusselt number) is weakly suppressed in the central zone of the lower wall with a four-fold change in AR. The effect is weak but non-trivial. Further calculations may be required which examine a wider range of AR values and also different types of geometry (triangular, elliptic, and circular) for different fluids also. Overall however good results have been obtained which provide a solid insight into the performance of the collector.

Case IV: Natural convection with radiation

The P1 flux model incorporates *optical thickness (τ_0), a* key radiative property, on thermofluid characteristics. In the vast majority of radiative-convective studies, optical thickness is assumed to be either very small (optically thin approximation) or very large (optically thick approximation). The latter results in a Rosseland-type diffusive

flux model. These extreme values of optical thickness are not representative of real media in solar collectors. More robust values correlating with solar cell design fall between 0.1 and 1, and these are implemented in the present computations in Figure 23-24. As optical thickness (optical depth) increases, i.e. greater absorption coefficient, thermal radiation is better attenuated in the medium and this induces heating. Higher temperatures result at the base wall for the P1 model compared with the Rosseland model.

Optical thickness and absorption coefficient are dimensionless quantifications of how much a given medium retards the passage of thermal radiation. Radiative intensity falls by an exponential factor when optical thickness is unity. Physically optical thickness will be a function of absorption coefficient, medium density and propagation distance.

The P1 model better predicts the actual influence of solar radiative flux than the limited Rosseland model. Figure 25 shows that with increasing absorption coefficient the local convective heat flux decreases for the P1 model whereas it increases for the S2S (Rosseland) flux model.

6. CONCLUSIONS

Computational fluid dynamic simulations of two-dimensional laminar natural thermal convection and radiative heat transfer in solar collector enclosures have been presented using CFD software based on the finite volume method. Validation of the computations has also been included with a Marker-and-Cell finite difference algorithm. The accuracy of the CFD computations with a detailed mesh independence (grid dependence) study has also been conducted and comparisons made with published simulations. Important observations were made including the fact that different gases (air, ammonia) perform significantly differently in terms of localization or distribution of thermal energy in the base-wall heated solar collector. The simulations have shown that:

- As Rayleigh number is increased from *Ra=100 to Ra=1000* the lower heated zone near the base wall is expanded significantly. Heat flux penetrating the solar cell is enhanced.
- As Rayleigh number is increased, the dual thermal field structure computed in the solar cell evolves considerably although it is only truly formed at the highest Rayleigh number (Ra =10,000,0000).
- Higher temperatures result at the base wall for the P1 model compared with the Rosseland model.
- The P1 model generates more accurate results for the actual influence of solar radiative flux than the limited Rosseland model.

- As radiative absorption coefficient is increased the local convective heat flux increases for the S2S (Rosseland) flux model whereas it is reduced for the P1 model.
- Local convective flux is less influenced with aspect ratio than with the Rayleigh or Prandtl number.
- At higher Prandtl number (lower thermal conductivity of the solar collector fluid), a demonstrably more symmetric and stable dual bolus structure is observed; however local convective flux at the wall is suppressed as Prandtl number is elevated indicating that the choice of working gas is critical for sustaining high efficiency.

The present study has been restricted to *single-phase* transport phenomena. However recent developments in doping working fluids with nano-particles have shown considerable thermal enhancement. A logical extension to the current work is therefore the utilization of nanofluids as the working solar collector fluid [43].

Acknowledgements

The authors wish to express their gratitude to the reviewers who highlighted important areas for improvement in this article.

References

[1] Wertz JR, Wiley JL (1999) Space Mission Analysis and Design, Microcosm Press, El Segundo California, USA.

[2] Pisacane VL, Robert CM (1994) Fundamentals of Space Systems, Oxford University Press, New York, USA.

[3] Kreith F (1962) Radiation Heat Transfer: For Spacecraft and Solar Power Plant Design, International Textbook Company, University of California, USA.

[4] Yang WH, Cheng HE, Cai A (2004) Thermal analysis for folded solar array of spacecraft in orbit. Appl Thermal Eng, 24:595-607.

[5] Ostrach S (1988) Natural convection in enclosures. ASME J Heat Transfer, 110(4b):1175-1190.

[6] Aydm O (1999) Transient natural convection in rectangular enclosures heated from one side and cooled from above. Int Commun. Heat Mass Transfer, 26(1):135-144.

[7] Basak T, Roy S, Balakrishnan AR (2006) Effects of thermal boundary conditions on natural convection flows within a square cavity. Int J Heat Mass Transfer, 49:4525-4535.

[8] Bhargava R, Sharma S, Bhargava P, Anwar Bég O, Kadir A (2017) Finite element simulation of nonlinear convective heat and mass transfer in a micropolar fluid-filled enclosure with Rayleigh number effects. Int J Appl Comput Math, 3(2):1347–1379.

[9] Su Z, Gu S, Vafai K (2017) Modeling and simulation of ray tracing for compound parabolic thermal solar collector. Int Commun Heat and Mass Transfer, 87:169-174.

[10] Khoukhi M, Maruyama S, Sakai S, Behnia M (2003) Combined non-gray radiative and conductive heat transfer in solar collector glass cover. Solar Energy, 74: 285-293.

[11] Lee BJ, Park K, Walsh T, Xu L (2012) Radiative heat transfer analysis in plasmonic nanofluids for direct solar thermal absorption. ASME J Solar Energy Eng, 134(2): Article ID: 021009.

[12] Anwar Bég O, Ferdows M, Bég TA, Ahmed T, Wahiduzzaman M, Alam MM (2016) Radiative optically-dense magnetized transient reactive transport phenomena with cross diffusion and dissipation effects: numerical simulations. J Taiwan Inst Chem Eng, 66:12–26.

[13] Anwar Bég O, Zueco J, Bég TA, Takhar HS, Kahya E (2009) NSM analysis of time-dependent nonlinear buoyancy-driven double-diffusive radiative convection flow in non-Darcy geological porous media. Acta Mechanica, 202:181-204.

[14] Moufekkira F, Moussaoui MA, Mezrhub A, Naji H, Lemonnier D (2012) Numerical prediction of heat transfer by natural convection and radiation in an enclosure filled with an isotropic scattering medium. J Quantitative Spectroscopy and Radiative Transfer, 113(13):1689-1704.

[15] Mondal B, Li X (2010) Effect of volumetric radiation on natural convection in a square cavity using lattice Boltzmann method with non-uniform lattices. Int J Heat and Mass Transfer, 53(21):4935-4948.

[16] Liu X, Gong G, Hengsheng C (2014) Combined natural convection and radiation heat transfer of various absorbing-emitting-scattering media in a square cavity. Adv Mech Eng, 6:1-10.

[17] Rabhi M, Bouali H, Mezrhab A (2008) Radiation–natural convection heat transfer in inclined rectangular enclosures with multiple partitions. Energy Conv. Management, 49:228-1236.

[18] Anwar Bég O, Ali N, Zaman A, Bég TA, Sohail A (2016) Computational modelling of heat transfer in annular porous medium solar energy absorber with a P1-radiative differential approximation. J Taiwan Inst Chem Eng, 66: 258-268.

[19] Bouali H, Mezrhab A, Amaoui H, Bouzidi M (2006) Radiation-natural convection heat transfer in an inclined rectangular enclosure. Int J Thermal Sci, 45:553-566.

[20] Nouanegue HF, Muftuoglu A, Bilgen E (2009) Heat transfer by natural convection, conduction and radiation in an inclined square enclosure bounded with a solid wall. Int J Thermal Sci, 48:871-880.

[21] Kuznetsov GV, Sheremet MA (2009) Conjugate natural convection with radiation in an enclosure. Int J Heat and Mass Transfer, 52:2215-2223.

[22] Moufekkir F, Moussaoui MA, Mezrhub A, Lemonnier D, Naji H (2012) MRT-lattice Boltzmann computations of natural convection and volumetric radiation in a tilted square enclosure. Int J Thermal Sci, 54:125-141.

[23] Mejri I, Mahmoudi A, Abbassi MA, Omri A (2016) LBM simulation of natural convection in an inclined triangular cavity filled with water. Alexandria Eng J, 55:1385-1394.

[24] ANSYS FLUENT Version 17.2 (2017) Theory Guide, Lebanon, New Hamp., USA.

[25] Kuharat S (2017) Simulation of natural convection in enclosure-based spacecraft solar collector systems, MSc Dissertation, Aerospace Engineering, Department of Aeronautical and Mechanical Engineering, University of Salford, Manchester, UK, September (99 pages).

[26] Sze CNP, Hughes BR, Anwar Bég O (2011) Computational study of improving the efficiency of photovoltaic panels in the UAE, ICFDT 2011-International Conf. Fluid Dynamics and Thermodynamics, Dubai, UAE, January 25-27.

[27] Dombrovsky LA (2012) The use of transport approximation and diffusion-based models in radiative transfer calculations. Comput. Therm. Sci, 4: 297–315.

[28] Dombrovsky LA, Baillis D (2010) Thermal Radiation in Disperse Systems: An Engineering Approach. Begell House, New York.

[29] Satya Narayana PV., Akshit SM, Ghori JP, Venkateswarlu B (2017) Thermal radiation effects on an unsteady MHD nanofluid flow over a stretching sheet with non-uniform heat source/sink. J. Nanofluids, 6:899-907.

[30] Rana S, Mehmood R, Satya Narayana PV, Akbar NS (2016) Free convective nonaligned non-Newtonian flow with non-linear thermal radiation. Commun. Theor. Phys, 66:687–693.

[31] Harlow FH, Welch JE (1965) Numerical calculation of time-dependent viscous incompressible flow of fluid with free surface. Physics of Fluids, 8:2182-2190.

[32] M. Modest M (1992) Radiative Heat Transfer, MacGraw-Hill, New York.

[33] Chandrasekhar S (1960) Radiative Transfer, Oxford University Press, New York.

[34] Bhatti MM, Shahid A, Anwar Bég O, Kadir A (2017) Numerical study of radiative Maxwell viscoelastic magnetized flow from a stretching permeable sheet with the Cattaneo–Christov heat flux model. Neural Comput& Applic, https://doi.org/10.1007/s00521-017-2933-8.

[35] Koenig HA (1998) Modern Computational Methods, Taylor and Francis, USA.

[36] Daud HA, Li Q, Anwar Bég O, Ghani SA (2010) CFD modeling of blowing ratio effects on 3-D skewed gas turbine film cooling, 11th Int. Conf. Advanced Comput. Methods and Exp. Measurements in Heat Transfer, Tallinn, Estonia, 14-16 July.

[37] Barth TJ, Jespersen D (1989) The Design and Application of Upwind Schemes on Unstructures Meshes. AIAA 27th Aerospace Sciences Meeting, Nevada, USA.

[38] Taoufik N, Jamil Z, Rajeb BM (2013) Lattice Boltzmann analysis of 2-d natural convection flow and heat transfer within square enclosure including an isothermal hot block. Int J Thermal Tech, 3:146-154.

[39] Taoufik N, Ridha D (2012) Natural convection flow and heat transfer in square enclosure asymmetrically heated from below: A lattice Boltzmann comprehensive study. Computer Modelling in Eng Sci, 88(3): 211-227.

[40] Oh J, Ha M, Kim K (1997) Numerical study of heat transfer and flow of natural convection in an enclosure with a heat generating conducting body. Numerical Heat Transfer: Part A, 31: 289-304.

[41] M. Paroncini, F. Corvaro, Natural convection in a square enclosure with a hot source, Int J Thermal Sci 48 (2009) 1683-1695.

[42] Duffie JA, Beckman WA (2013) Solar Engineering of Thermal Processes, 4th Edition, Wiley, New York.

[43] S. K. Das, S. U. S. Choi, W. Yu, T. Pradeep (2007), Nanofluids: Science and Technology, John Wiley, New York, USA.

TABLES

Table 1: Thermophysical properties adopted in ANSYS simulation

Prandtl number (Pr)	0.7
Rayleigh number (Ra)	1000
Density (ρ) kg/m^3	0.89754
Thermal expansion coefficient 1/K	2.00E-03
Gravity (g) m/s^2	9.81
Kinematic viscosity (v) m^2/s	2.52E-05
Conductivity (K)	0.0326
Specific Heat (Cp)	1.01E+03

Table 2: Mesh numerical experiments

	Case 1	Case 2	Case 3	Case 4	Case 5
Number of Element	525	1785	6060	12835	22110
Number of Node	572	1700	5900	12600	21800

Table 3: ANSYS FLUENT Mesh dependency information

	Case 1	Case 2	Case 3	Case 4	Case 5
Number of divisions in y direction	25	50	100	200	250
Number of divisions in x direction	12	25	50	100	125
number of elements	525	1785	6060	22110	33750
number of node	572	1700	5900	21800	34136

Table 4: Grid Sensitivity Analysis

Order of the Scheme *a*	Discretization Error ε_h^d *W m^-2*	Finest mesh Solution $\emptyset_h$ *W m^-2*	Richardson Solution Φ *W m^-2*
0.3141	0.01	1.6551	1.6491

FIGURES

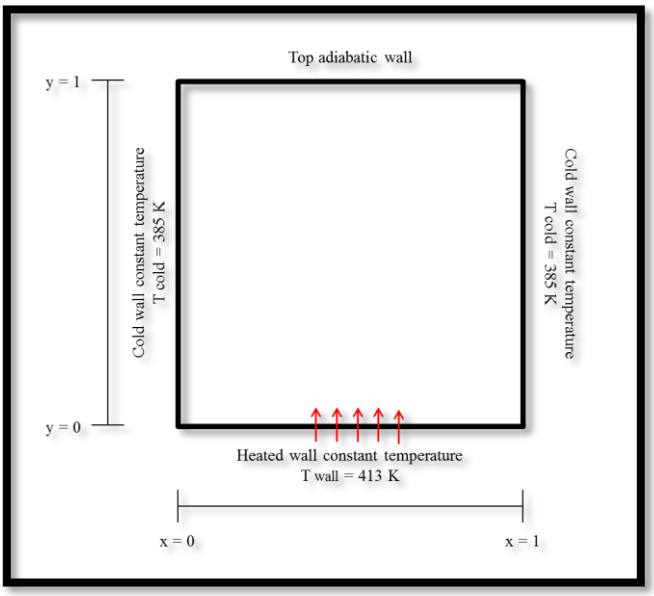

Figure 1: Solar collector geometrical model

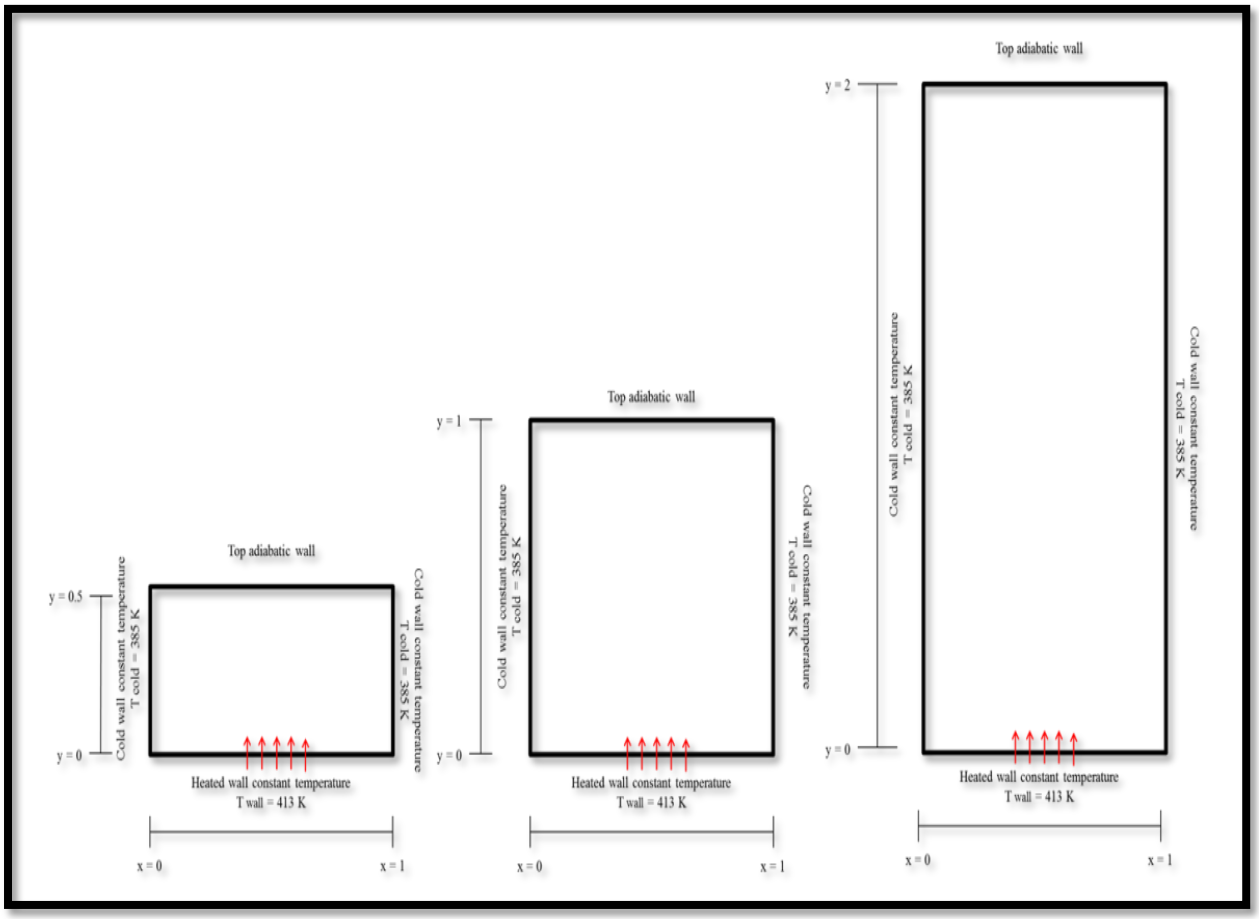

Figure 2. Enclosure geometries for various aspect ratios

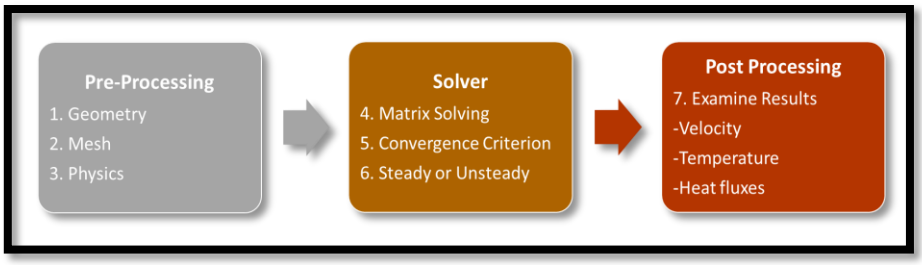

Figure 3. ANSYS FLUENT simulation methodology

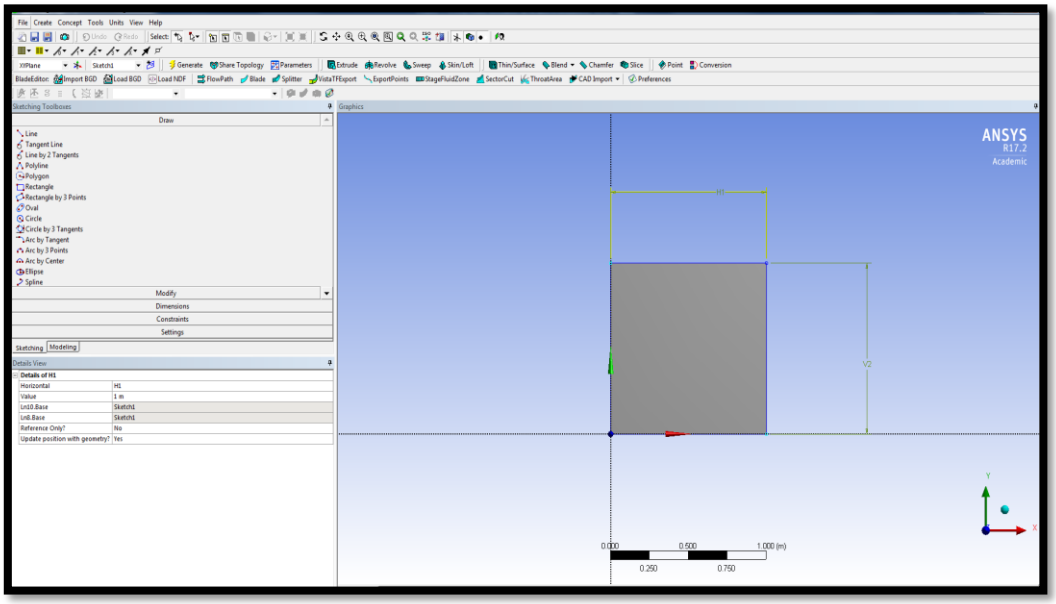

Figure 4. ANSYS geometry definition

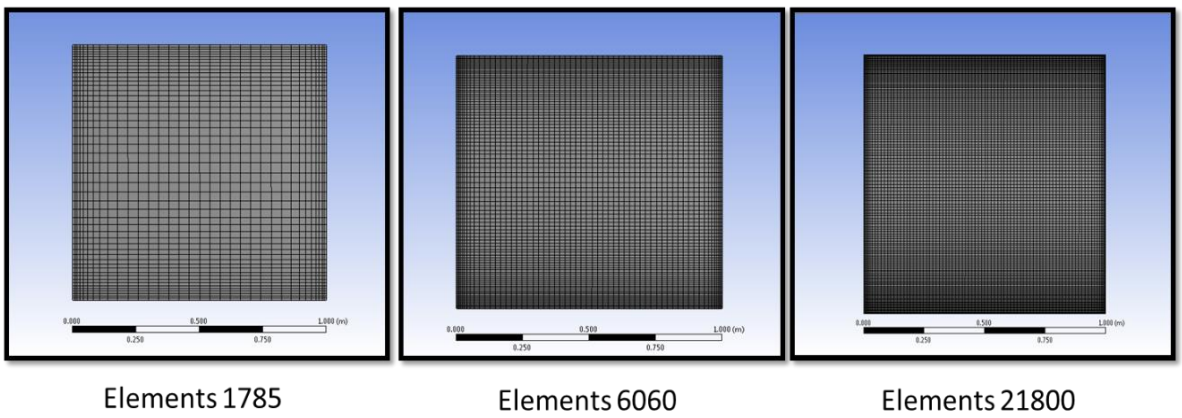

Figure 5. Mesh Structures

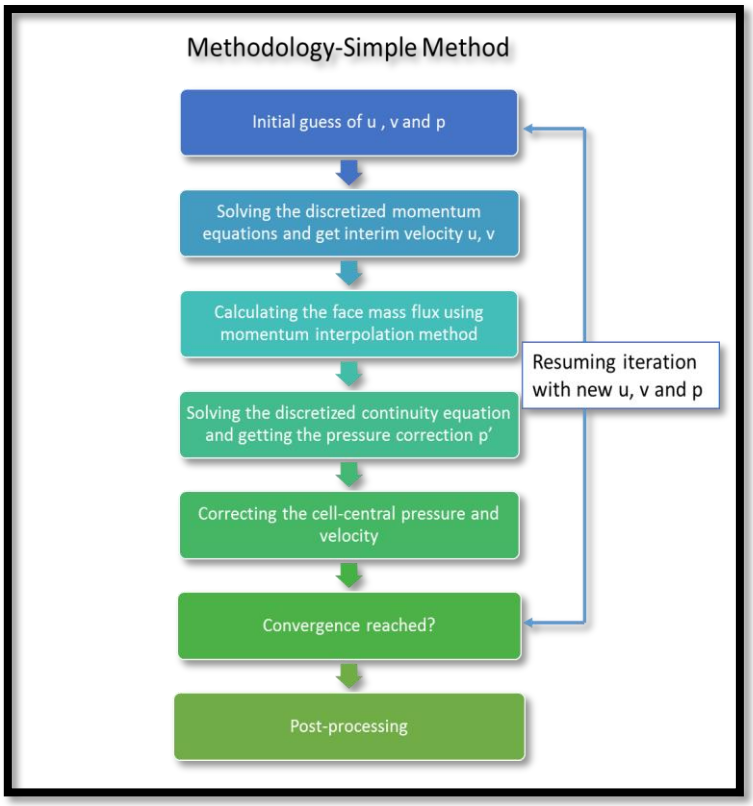

Figure 6. Methodology of ANSYS FLUENT Simple algorithm

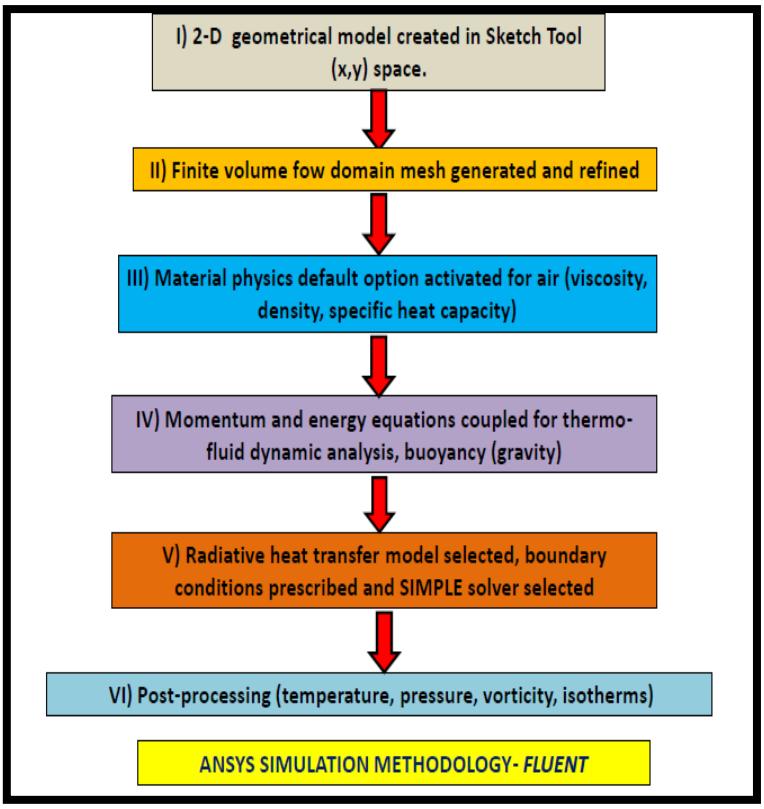

Figure 7. ANSYS FLUENT simulation approach

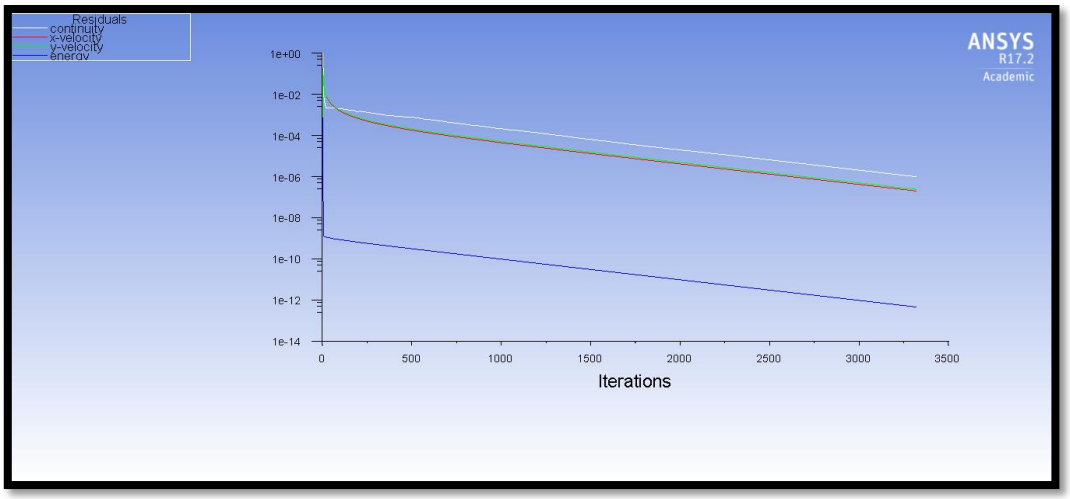

Figure 8. Residual monitoring

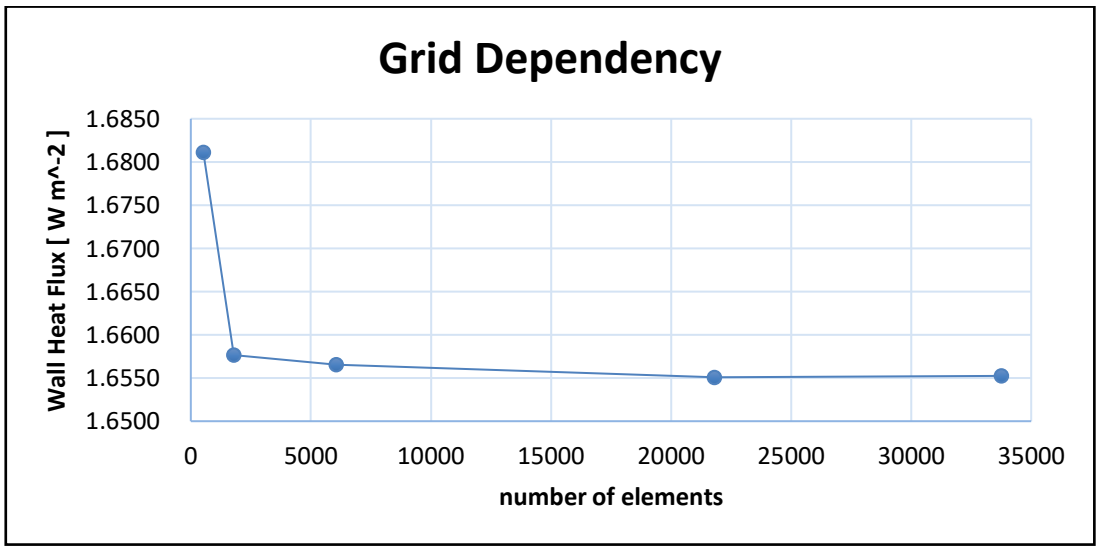

Figure 9. Grid Dependency

Fig 10

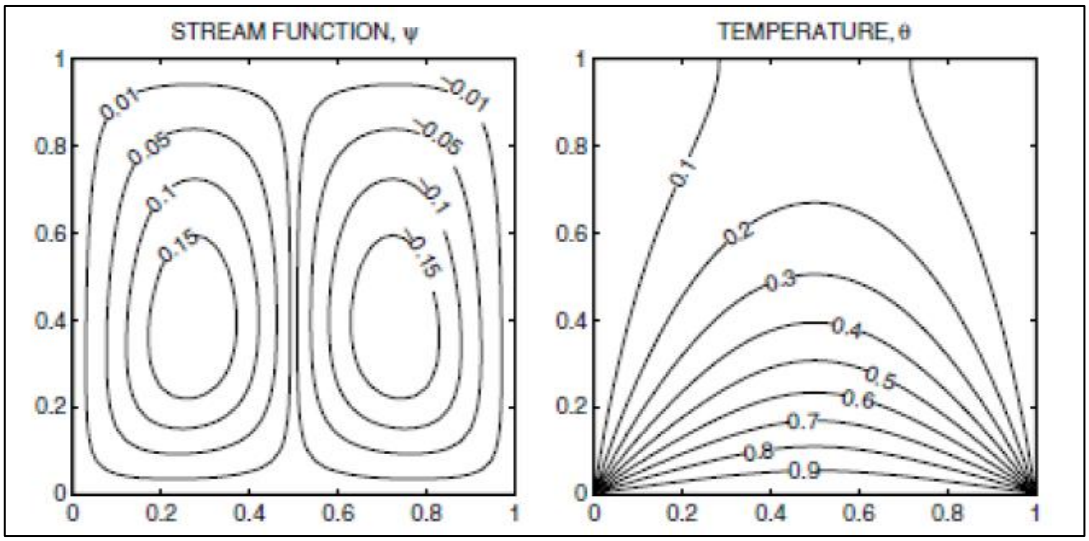

Fig 11

Figure 10 (left) : Streamline solutions of Basak et al. [**7**] (Pr=0.7, Ra = 10^3) and **Figure 11 (right) :** Temperature contour solutions of Basak et al. [**7**] (Pr=0.7, Ra = 10^3)

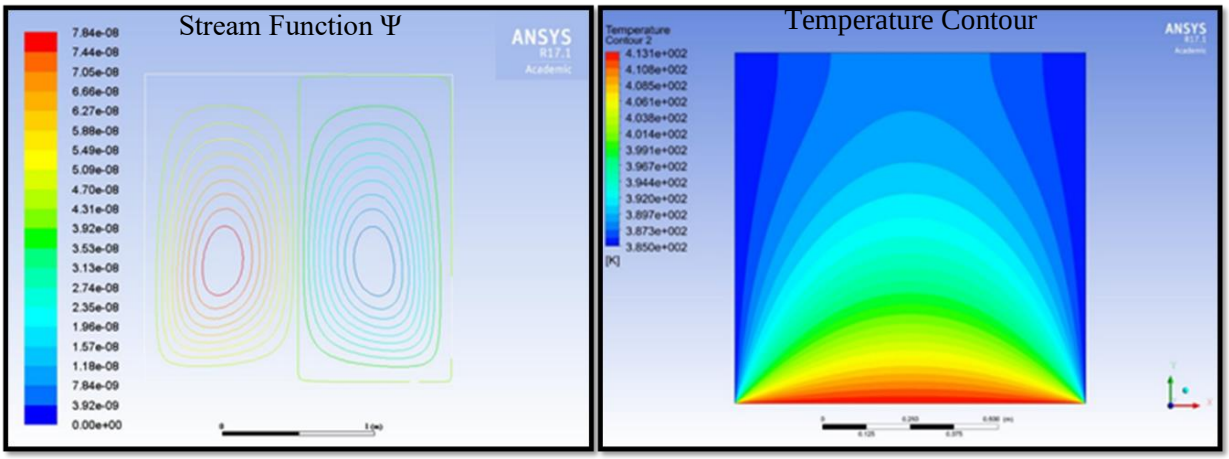

Figure 12 : ANSYS FLUENT CFD simulation results (Pr=0.7 Ra=10^3)

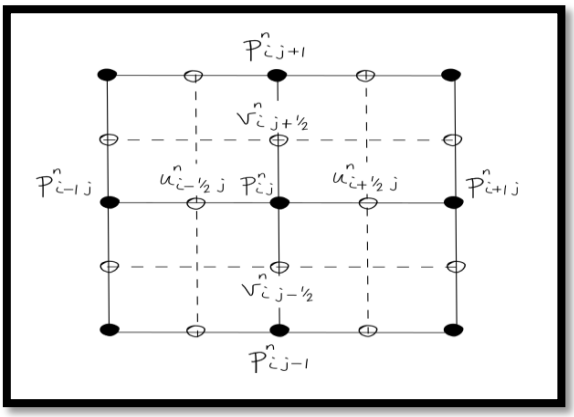

Figure 13: Marker and Cell (MAC) discretization method

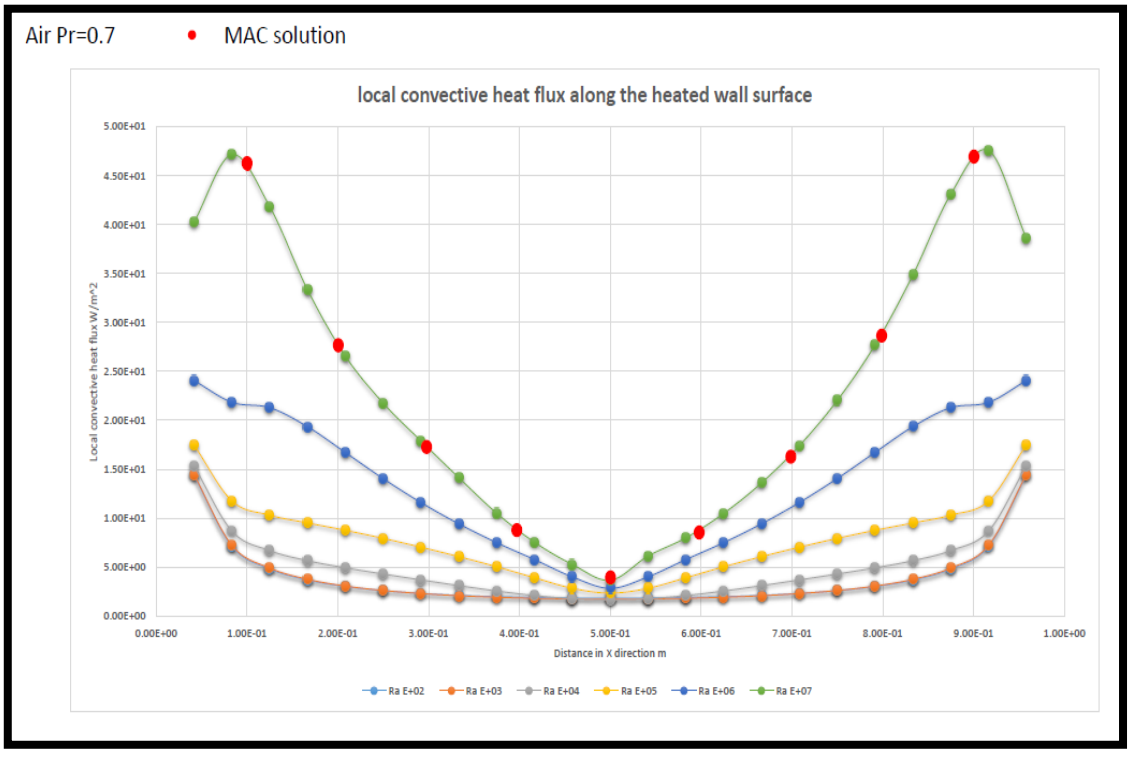

Figure 14: ANSYS FLUENT and MAC Comparison

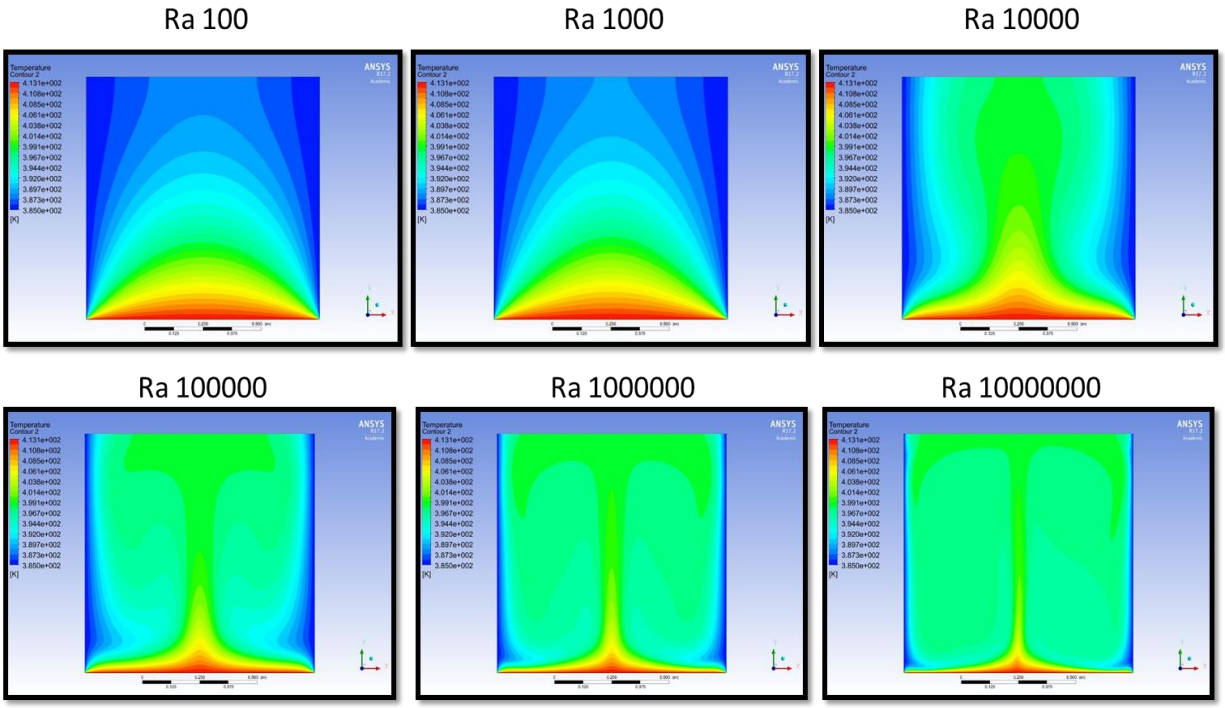

Figure 15: Temperature contours for different Rayleigh numbers

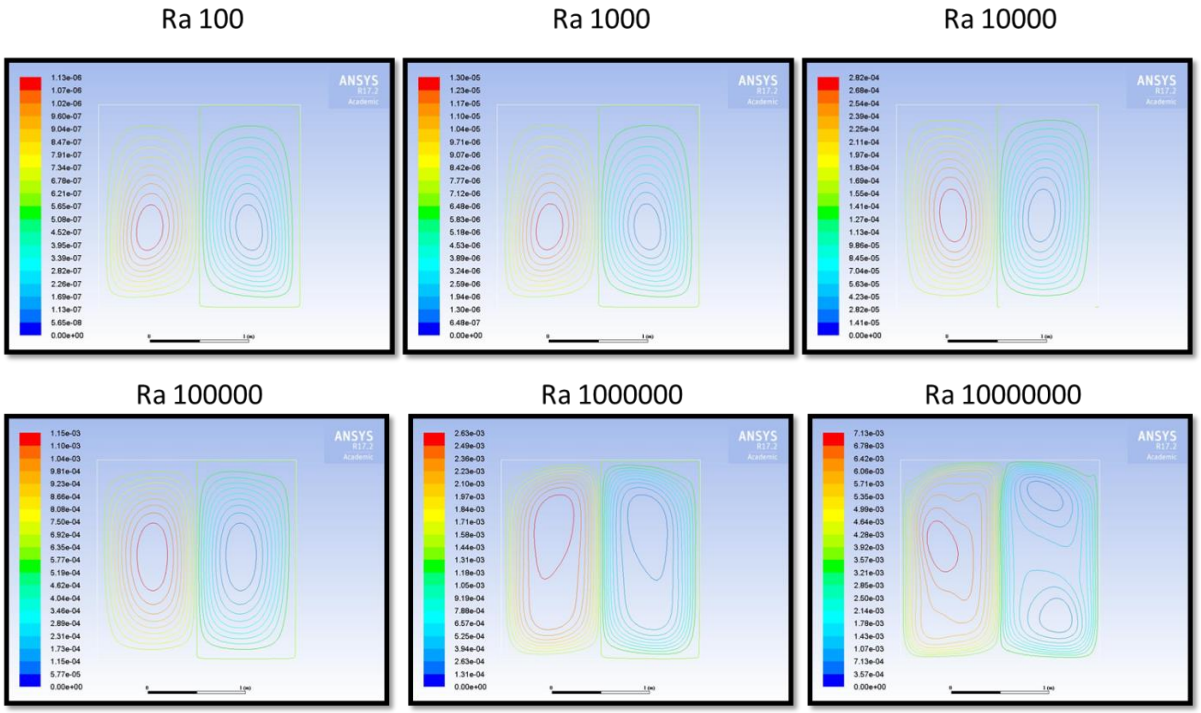

Figure 16: Stream Function (Ψ) for different Rayleigh numbers

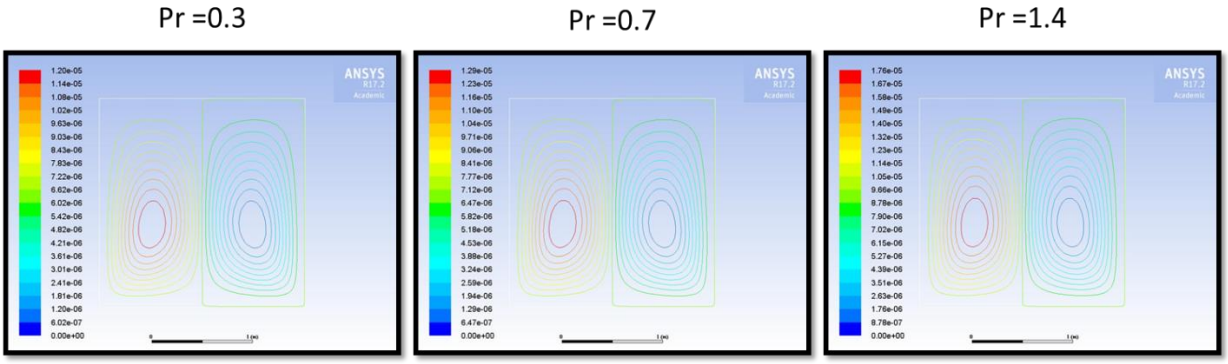

Figure 17: Stream Function (Ψ) variation with varying Prandtl numbers

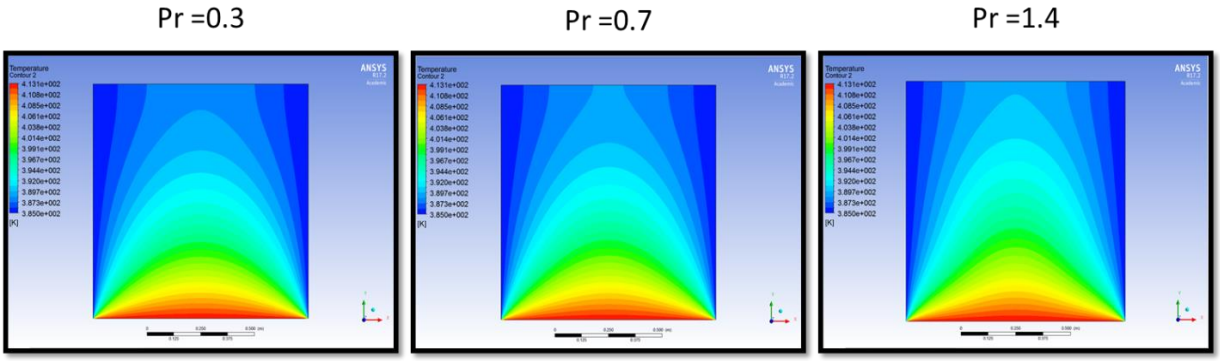

Figure 18: Temperature contours with varying Prandtl numbers

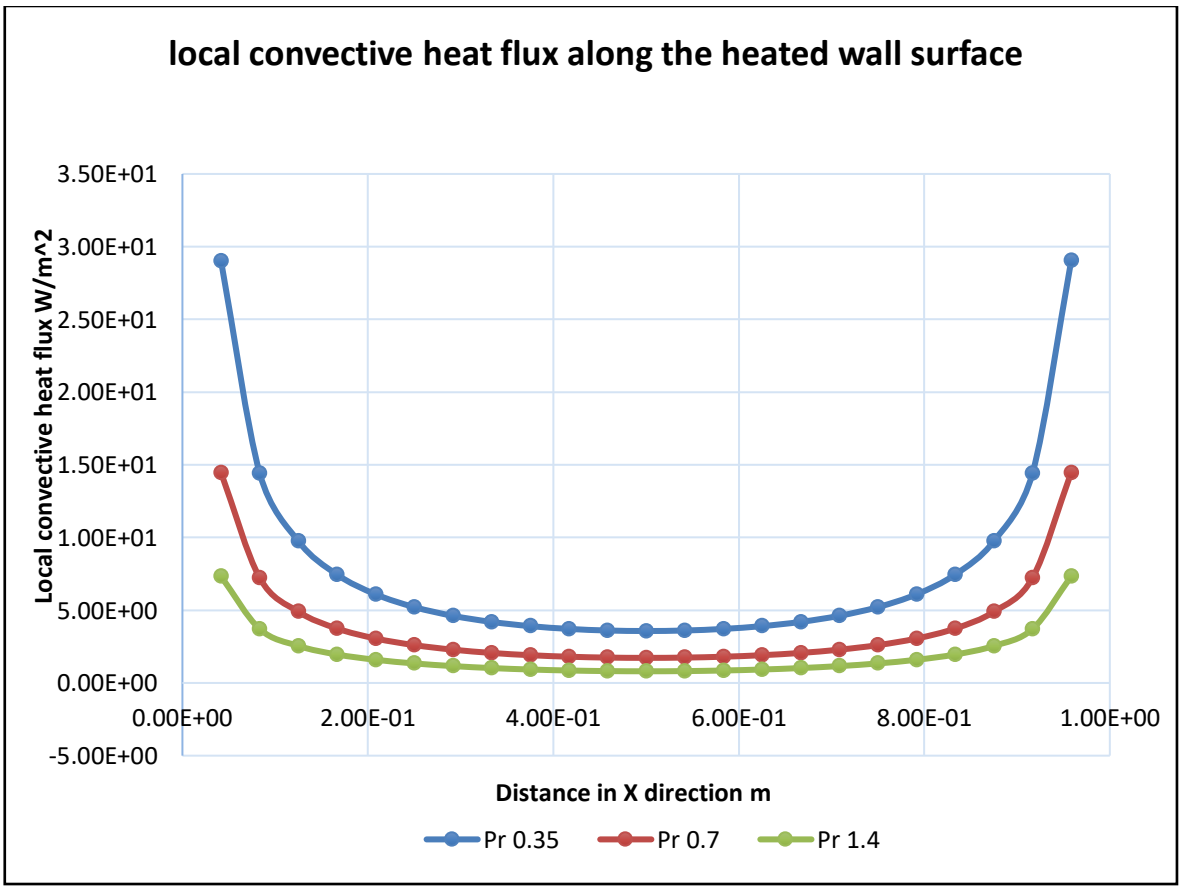

Figure 19: Local convective heat flux along heated wall surface with Prandtl numbers

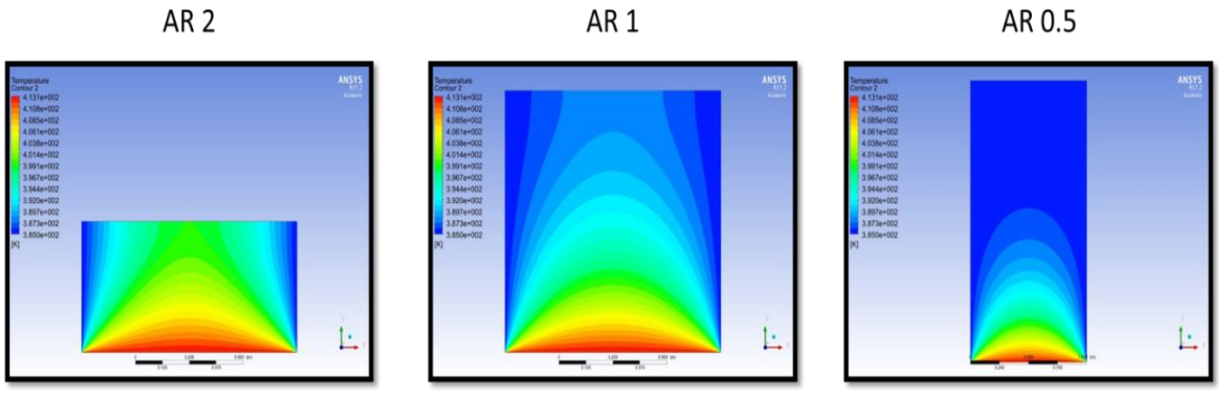

Figure 20: Temperature contours for different aspect ratios

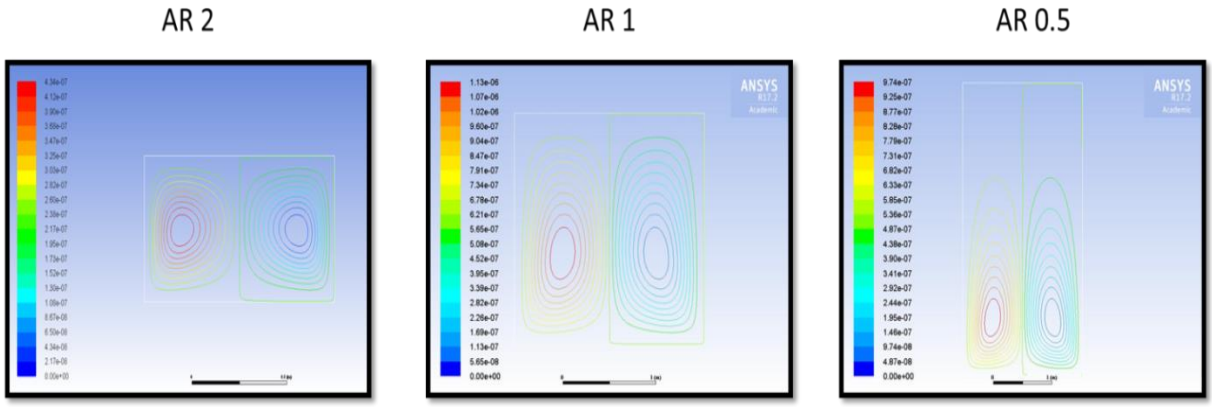

Figure 21: Stream function (Ψ) plots for different aspect ratios

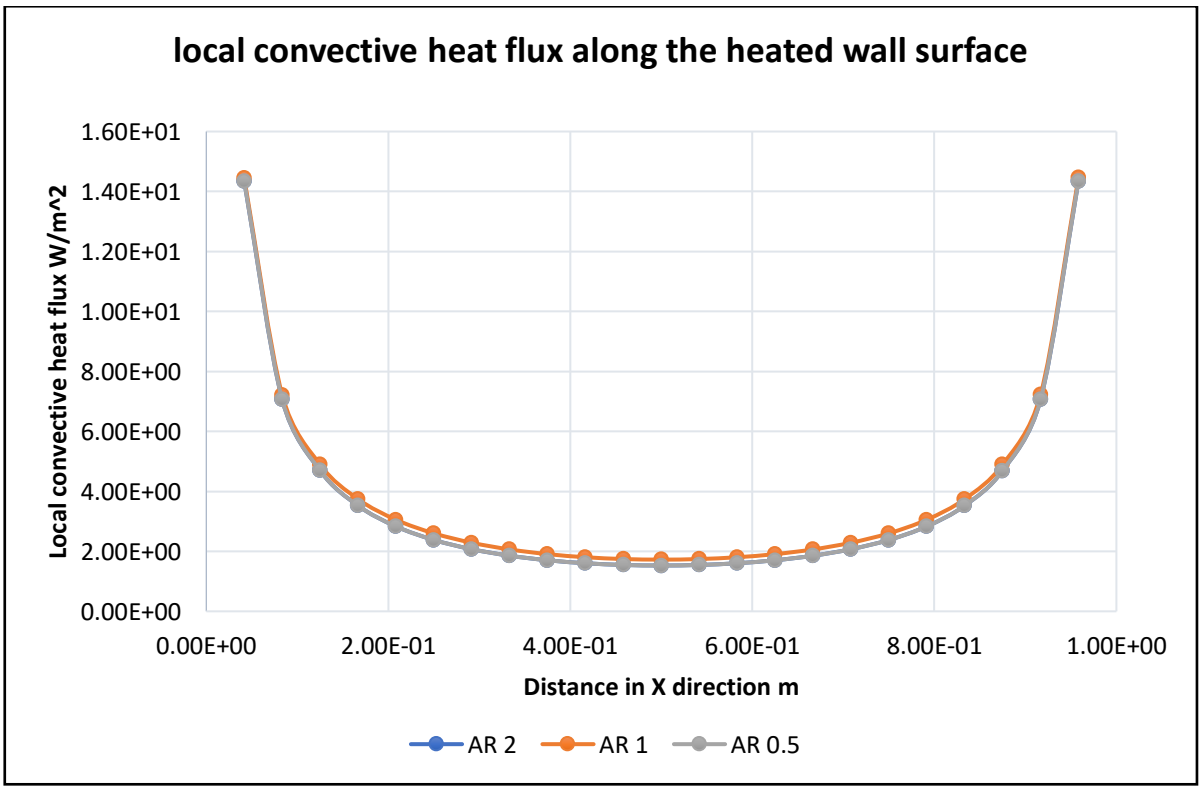

Figure 22: Local convective heat flux along heated wall surface with aspect ratio

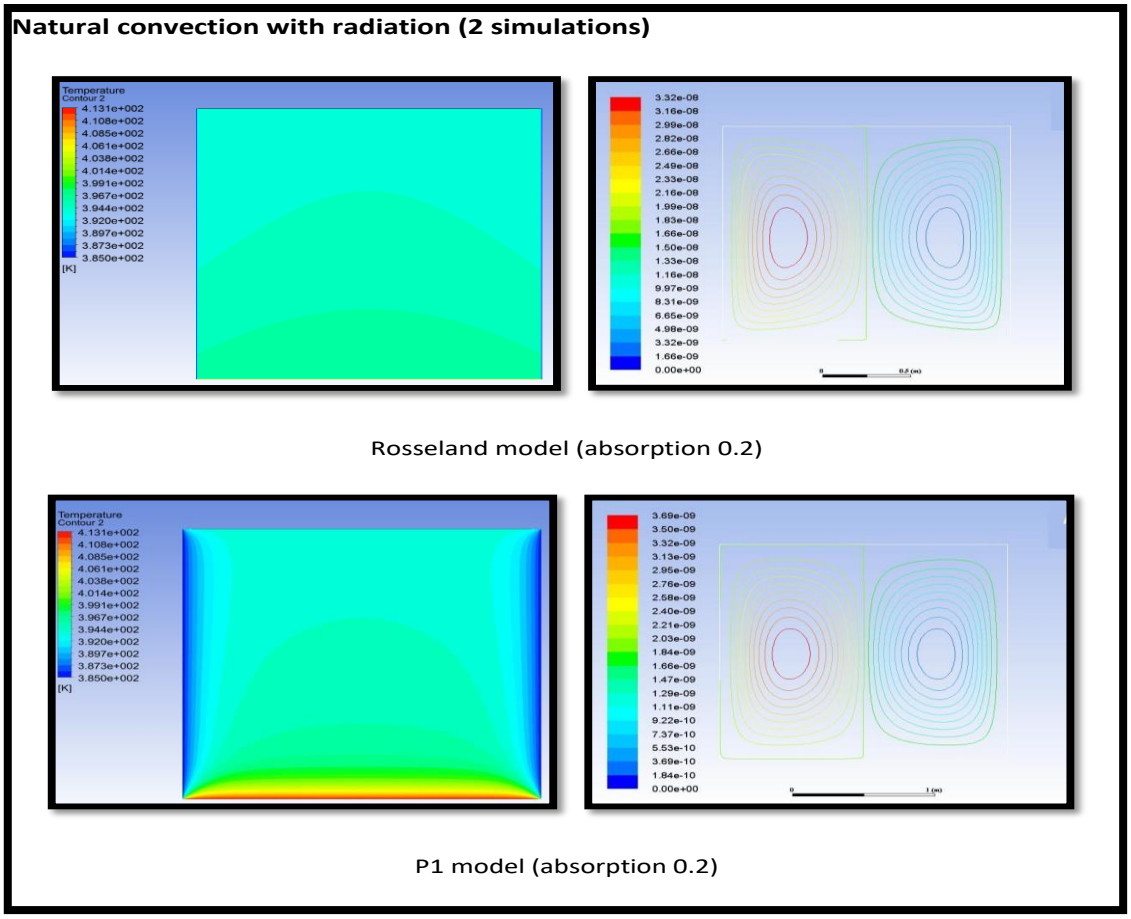

Figure 23: Temperature and isotherm plots with different radiative flux models (low absorption)

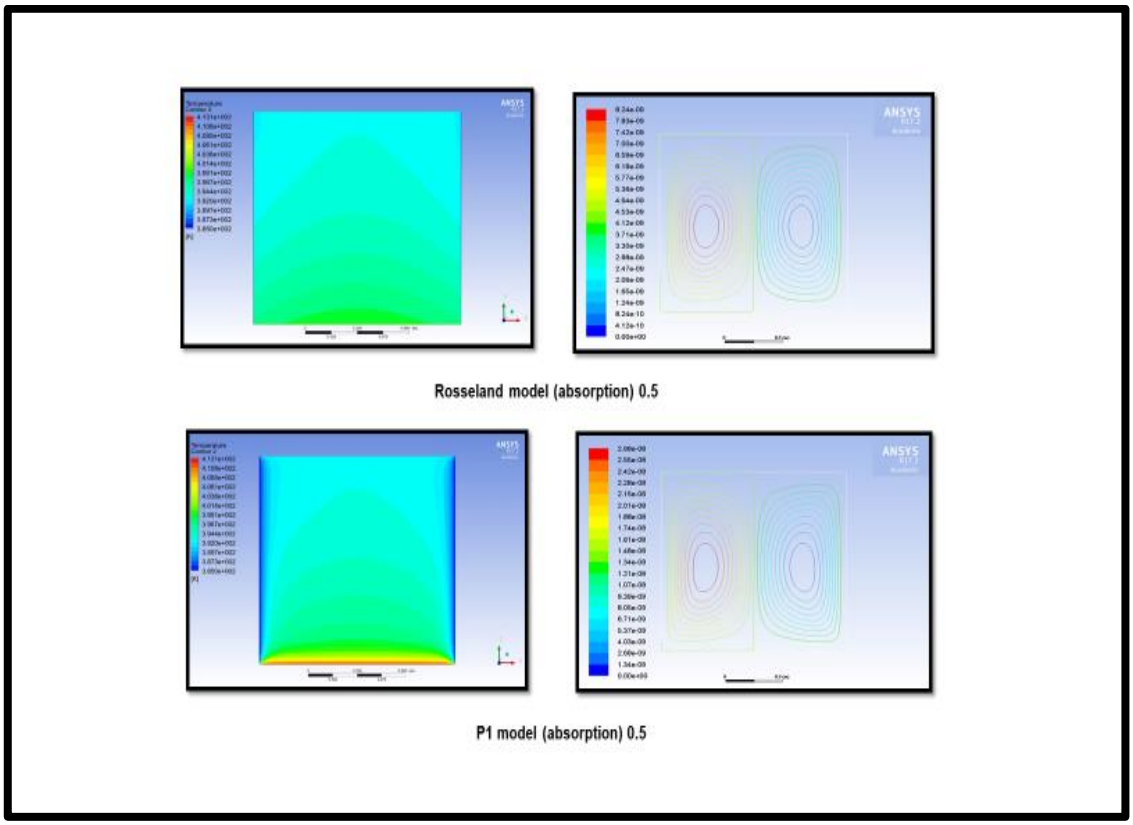

Figure 24: Temperature and isotherm plots with different radiative flux models (high absorption)

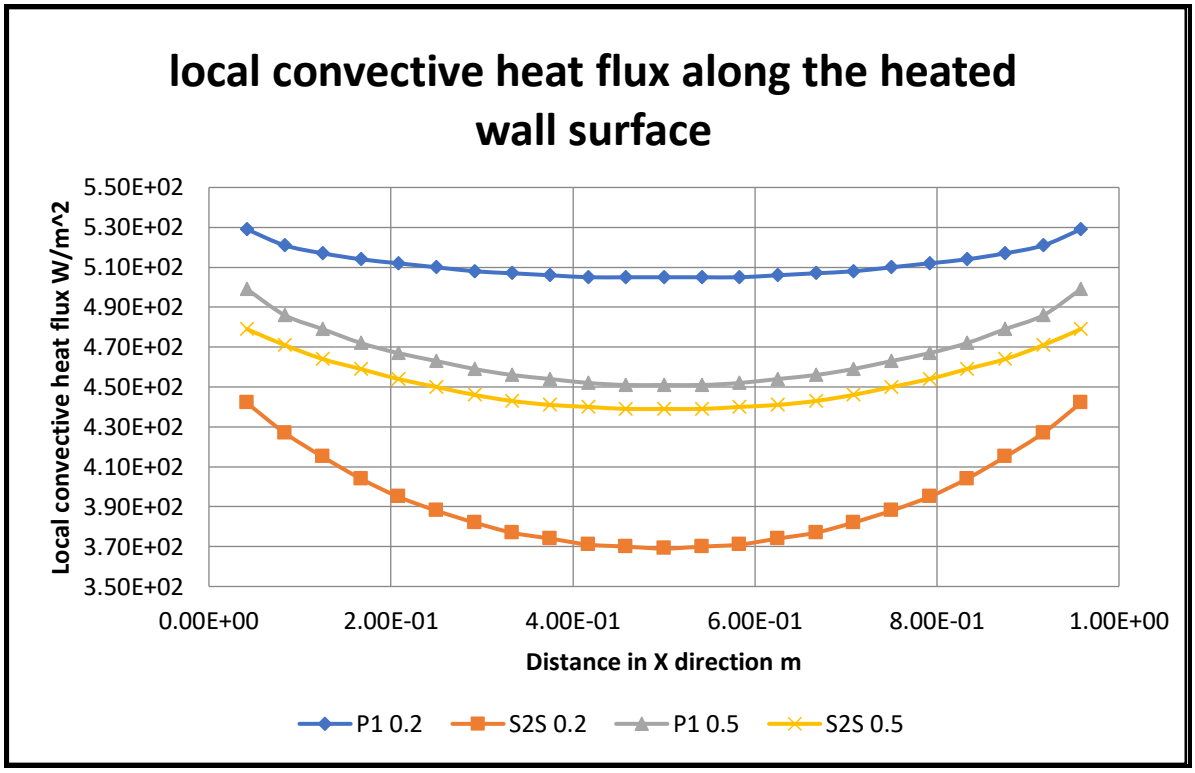

Figure 25: Local convective heat flux along heated wall surface (varying absorptions)